



3D Printing of high melting iron alloys using metal-fused deposition modeling: a comprehensive review

Matthew Drummond¹ · Abdelkrem Eltaggaz¹ · Ibrahim Deiab¹

Received: 1 June 2023 / Accepted: 17 August 2023 / Published online: 14 September 2023
© The Author(s), under exclusive licence to Springer-Verlag London Ltd., part of Springer Nature 2023

Abstract

Advancements in additive manufacturing (AM) have allowed for a transition in the manufacturing industry. The ability to print solid metal parts for use in prototypes, custom tooling, and fast replacement parts has driven advancements in the manufacturing sector. Material extrusion additive manufacturing processes such as fused deposition modeling (FDM) is a common AM processes in the world of thermoplastics and it is being developed in the field of metal additive manufacturing. Metal FDM (FDMm) process provides a low cost, customizable, and user-friendly printing experience while still delivering high printing tolerances. While there are many materials that can be printed using FDM technologies, process parameters vary across materials resulting in inconsistent process parameters across the industry. This review paper focuses on the techniques and parameters performed by various researchers for the printing, debinding, and sintering of FDM printed 316L Stainless Steel, 17-4PH Stainless Steel and high melt Iron alloy filaments.

Keywords Additive Manufacturing · Metal FDM · 3D Printing · 316L Stainless Steel · 17-4 Stainless Steel

1 Introduction

Additive manufacturing (AM) technology is changing the subtractive manufacturing field. AM builds a part up layer by layer instead of traditionally starting with a bulk piece removing material down to the desired part [1]. Additive manufacturing uses a 3-dimensional computer aided design (CAD) model to create a part in one machine instead of many unique operation machines. This allows for the creation of quick, one-off prototypes created directly from a CAD model with little manual intervention [1, 2]. Additive manufacturing applications span across a vast number of industries such as the automotive, agricultural, aerospace, and medical [3–5]. Currently, metal AM is being used in the manufacturing industry to create unique custom parts such as custom tooling, cast mold creation, incorporation of complex geometries into existing parts and developing legacy parts for automobiles no longer in production [6, 7]. As metal 3D printing advances, it is set to take over the subtractive manufacturing sector with increasing tolerances,

reductions in waste and manual labor cost while creating an energy-efficient and cost-effective solution to manufacturing [8, 9].

While metal AM is in its earliest stages, many new methods and materials are being developed and tested. AM offers printing capabilities for a range of materials such as ceramics, high melt metal alloys, low melt metal alloys, thermoplastics bioplastics, resins and many more [5, 10, 11]. Materials such as stainless steel, titanium, bronze, and copper have been experimentally printed and analyzed with promising results [8]. Currently, common metal AM technologies include powder bed fusion, direct energy deposition, binder jetting, bound powder extrusion and fused deposition modeling [12, 13]. Many of those AM technologies have expensive setup and operating costs while suffering from a complex operating procedure [14]. Fused filament fabrication (FFF), fused deposition modeling (FDM), and atomic diffusion additive manufacturing (ADAM) are inexpensive compared to other AM technologies as they provide the opportunity for both industry and hobbyists to manufacture relatively cheap metal parts [15]. Low cost fused deposition modeling was introduced around 2005 with commercialization of the idea in 2013 by Statasys Inc. [16]. Fused filament fabrication processes were developed to bypass Statasys patented “Fused deposition modeling (FDM)” terminology

✉ Matthew Drummond
MDrummond00@hotmail.com

¹ School of Engineering, University of Guelph, Guelph, Canada

[17]. Atomic diffusion additive manufacturing is a metal additive manufacturing process patented by Markforged which uses a “plastic-bound metal powder” to produce high precision metal parts [18–20]. The inclusion of metallic powder within the thermoplastic filament allows for FDM/FFF/ADAM technologies to successfully print metal. Fused deposition modeling, FFF, and ADAM all essentially provide the same AM process by extruding metal-infused thermoplastic into the desired print [15]. Thus, from this point forward fused deposition modeling, FDM and Metal FDM (FDMm) will be a generalization of the three processes. Metal FDM 3D printing follows 4 basic steps: splice, print, debind, and sinter [21].

Splicing happens within the virtual 3D CAD model. The CAD model is processed through a splicing software creating a G-Code file which tells the 3D printer how to print the part [22]. Within the splicing software, adjustments can be made to parameters such as infill percentage, support application, scale, shell thickness, layer height, flow rate percentage, raster angle, print speed and many more [22].

FDMm printing is typically done using industrial 3D printers designed for metal printing or by modifying a hobby thermoplastic printer to print metallic filament [23]. Industrial FDM printers are produced by companies such as Desktop Metal, Markforged and Rapidia, which provide faster and efficient FDMm printing solutions; however, high cost, limited material selection and customizability can hinder their use [24–28]. Hobby printing manufacturers such as Creality, Anycubic and Prusa sell convertible FDM printers starting around \$160 USD [29–31]. Upgrading to a direct drive extrusion system, hardened steel nozzle and filament support system can convert a typical hobby printer to a metal FDM printer [32]. In metal FDM filament, fine metal powder is infused into a printable thermoplastic [33]. Due to the inclusion of thermoplastic in the filament, standard FDM 3D printers can print metal filament into a high detail metal part. Metal FDM printing using hobbyist printing conversion is a cheap and customizable alternative compared to a commercial printer; however, there is a loss in print consistency, print speed, and technical support compared to industrial level printers.

Once printing is complete, it must undergo debinding process where its thermoplastic binder is removed before fusing the metal powder together [34]. Debinding is completed before the part is fully sintered. Debinding rates, temperature and environment type can all play a major factor in the effectiveness of the debinding and the quality of the final part [35]. The thermoplastic is typically removed using catalytic debinding or thermal debinding. Catalytic debinding uses a flow of inert gas within the sintering process to remove the binders as the kiln sinters the part [36]. Thermal debinding is incorporated into the sintering process and removed the binder through thermal vaporization [37]. The filaments binder is essential for the

successfulness part. A good binder provides flexibility when printing for bed adhesion, strength and must be able to either thermally or chemically debind [21].

The next step is to sinter the part. Sintering fuses the metallic powder in the part together, creating the final metal part [38]. Parts are typically sintered in a furnace in an open environment (typically inert) or enclosed in sintering refractory ballast and sintering carbon. The refractory ballast is a very fine powder with a high melting temperature to help retain the shape of the print during sintering [39]. Sintering carbon is often added on top of the refractory ballast to prevent carbon evaporation during sintering if not using an inert environment [40]. The sintering cycle varies based on the printed material and the size of the print. The temperature is raised to the sintering temperature, this is where the metallic powder fuses together to create the final metal part. After sintering, the refractory ballast can be filtered then reused and the parts are cleaned and machined if required. FDMm parts and metal AM parts in general can be subjected to additional heat treatment and post sintering processes to enhance their microstructure and mechanical properties [41, 42].

This literary review brings together research of process parameters and their results for high melt iron-based alloys. High melt iron alloys such as 316L stainless steel (SS) and 17-4PH stainless steel (SS) are commonly 3D printed using FDMm in order to remove the need for complex machining and/or casting processes. 316L stainless steel is commonly used in food and pharmaceutical grade infrastructure, heat exchangers, chemical processing and many parts that are exposed to water due to its inability to rust [43, 44]. 17-4PH SS has many applications in the aerospace, chemical processing and oil/petroleum refining industries due to its high strength [45, 46].

Individual research targeting select process parameters of metal FDM printing has been completed. However, there are no definite process parameters or starting points for additional research into the field. Bringing together information on FDM printed high melt iron alloy process parameters, successful research into parameter testing, and general knowledge about materials/methods used will accelerate the FDMm field and provide an adequate baseline for researchers entering the field. This review paper presents a comprehensive review about the process parameters used in FDMm high melt iron alloy research and highlights key/unique process parameter testing results. This review is split into three subsections: (1) Printing process: this section focuses on the metallic filament and printing parameters used in research to achieve a successful print. (2) Debinding process: this section focuses on the debinding process parameters and experimental into the debinding process. (3) Sintering process: this section provides key literary research on sintered microstructure, heat treatment, sintering processes data and mechanical properties.

2 Printing process

During FDM 3D printing, a thermoplastic filament is extruded through a heated nozzle from the printing head [47–49]. The thermoplastic filament is pulled by a stepper motor from a spool, fed through the drive system and out of the heated nozzle. The extruded thermoplastic is melted and sticks to the printers printing bed. The printing head transitions across the printing bed using an x-y coordinate system creating the first layer of the desired part. The printer deposits a base thermoplastic layer on the printing bed and

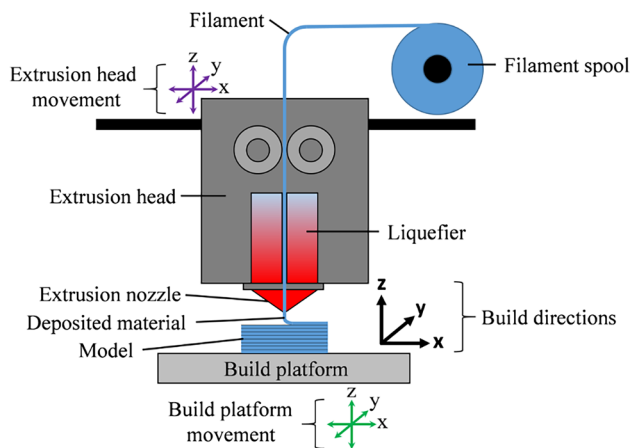
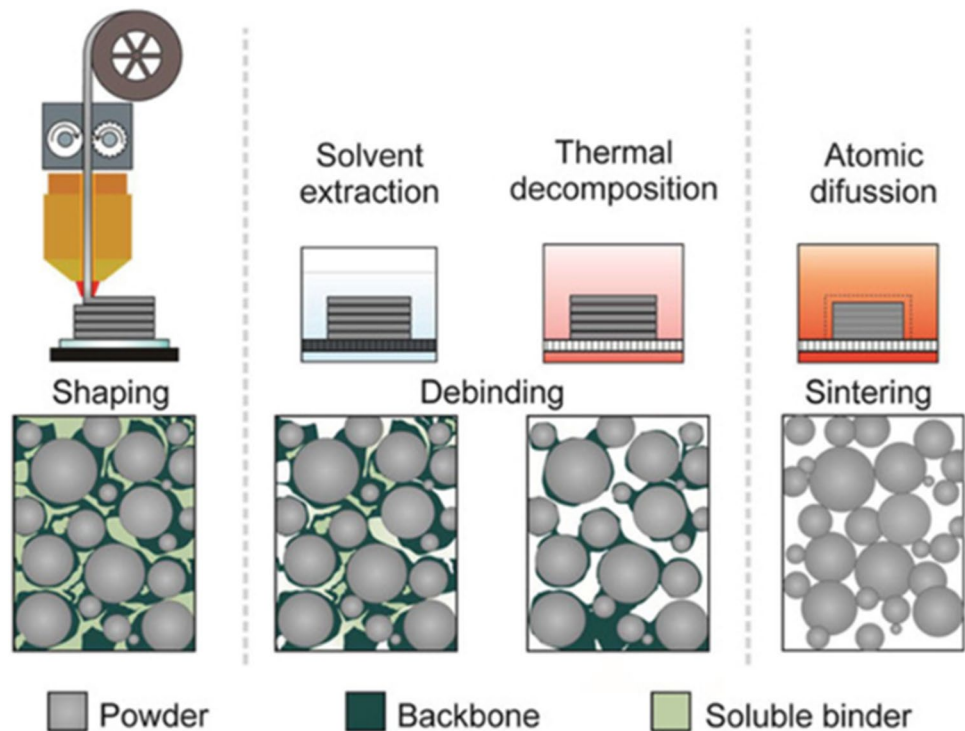


Fig. 1 Diagram of an FDM printing process [50]

Fig. 2 Binder during the FDMm process [56]



prints any additional layers on top of the already printed thermoplastic. Layer by layer, the printer builds up the part until a finished print is achieved [47–49]. Fig. 1 presents an FDM 3D printer system [50].

This section focuses on the metallic filament used in metal FDM printing and the printing process parameters for printing metal FDM. The goal of this section is to provide information on common metal filament and to investigate the printing parameters used for FDM printing of high melt iron alloys successfully.

2.1 Metallic Filament

FDMm filament is a printable thermoplastic infused with metallic particles. Commonly printed FDM thermoplastics such as polyethylene (PE), Polyoxymethylene (POM), Poly-lactic Acid (PLA), and Paraffin wax serve as binding agents for the metallic powder in the filament [48, 51–53]. Multiple binders can be mixed during the creation of filament, backbone binders 0–50 vol.% and soluble binders 50–90 vol.% with the rest being stabilizers and additives [54, 55]. The illustration done in Fig. 2 by Roshchupkin et al. [56] shows the binders interaction with the metallic powder.

The additive grade powder which is added to the binder tends to be sized between 20 and 80 μm [57]. The metallic powder content within the filament typically ranges from 50 to 65 vol.% with some materials up to 80% [58]. FDM filament is commonly made with a circular diameter of 1.75 mm or 2.85 mm [59]. From the literature reviewed in this study,

Table 1 Literature studies FDM filament information

Study	Material	Average powder size	Filament wt.%/vol.%
Mousapour et al. [35]	316L Stainless Steel	32 μm	83.5 wt.%
Wang et al. [42]	316L Stainless Steel	3–15 μm	80 wt.%
Nurhudan et al. [58]	316LX Stainless Steel	13 μm	88 wt.%
Nurhudan et al. [58]	316L Stainless Steel	17 μm	55 vol.%
Liu et al. [60]	316L Stainless Steel	30–50 μm	88 wt.%
Quarto et al. [61]	316L Stainless Steel	-	90 wt.%
Quarto et al. [61]	316L Stainless Steel	1–10 μm	-
Sadaf et al. [62]	316L Stainless Steel	33 μm	65 vol.%
Kurose et al. [63]	316L Stainless Steel	10 μm	60 vol.%
Hassan et al. [64]	316L Stainless Steel	-	63 vol.%
Damon et al. [65]	316L Stainless Steel	-	>80 wt.%
Thompson et al. [66]	316L Stainless Steel	17.7 μm	55 vol.%
Wagner et al. [67]	316L Stainless Steel	2.8 μm	-
Caminero et al. [68]	316LX Stainless Steel	1–20 μm	80 wt.%
Parenti et al. [69]	316L Stainless Steel	8.8 μm	92 wt.%, 60 vol.%
Lotfizarei et al. [70]	316L Stainless Steel	8.6 μm	-
Ortega et al. [71]	316L Stainless Steel	3–4 μm	-
Moritzer et al. [72]	316L Stainless Steel	-	90 wt.%
Gonzalez-Gutierrez et al. [73]	316L Stainless Steel	15.1 μm	55 vol.%
Burkhardt et al. [74]	316L Stainless Steel	-	55 vol.%
Nurhudan et al. [58]	17-4PH Stainless Steel	12 μm	55 vol.%
Lotfizarei et al. [70]	17-4PH Stainless Steel	12.3	-
Abe et al. [75]	17-4PH Stainless Steel	-	60 vol.%
Watson et al. [76]	17-4PH Stainless Steel	1–20 μm	-
Godec et al. [77]	17-4PH Stainless Steel	12.3 μm	55 vol.%
Gonzalez-Gutierrez et al. [78]	17-4PH Stainless Steel	12.3 μm	55 vol.%
Jiang and Ning [79]	17-4PH Stainless Steel	-	60 vol.%
Pellegrini et al. [80]	17-4PH Stainless Steel	-	90 wt.%
Pellegrini et al. [80]	17-4PH Stainless Steel	-	88 wt.%
Wu et al. [81]	17-4PH Stainless Steel	22 μm	58 vol.%
Gonzalez-Gutierrez et al. [73]	17-4PH Stainless Steel	12.3 μm	55 vol.%
Rahimi and Zamani [82]	4605 Steel	5 μm	90 wt.%
Vetter et al. [83]	1.2083 Tool Steel	-	60 vol.%
Mousapour et al. [35]	High Carbon Iron	129 μm	80 wt.%
Charpentier et al. [84]	High Carbon Tool Steel	45 μm	-

the filaments material, average powder size, and weight/volume percentage is listed in Table 1. It should be stated that binder type is not included as composition of the binder is often avoided in publications and patents [55].

2.2 Printing parameters

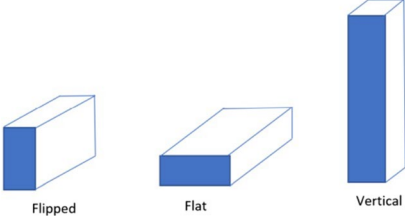
Although the FDM filament is made from commonly printed thermoplastics, the introduction of metallic powder into the filament changes the printing behavior. The slicing software offers adjustable printing parameters to customize the printer how the part. Certain printing parameters infill density and printing orientation are shown to have a significant effect on the mechanical properties of the printed part.

Table 2 reports the printing parameter terminology used within the literary studies.

Further in-depth analysis of the printing parameter testing, and printing parameters used to complete studies on FDM for high melt iron alloys can be viewed below in Table 3.

Quarto et al. [61] studied the effect of nozzle temperature, infill pattern, print speed and layer height on the density, shrinkage, and porosity of FDM printed 316L SS. A change in nozzle temperature showed no effect, whereas, higher print speed increased porosity and shrinkage of printed sample. Inversely, increasing the layer height marginally reduced the shrinkage rate by 17.5%. Ait-Mansour et al. [85] examined the compressive strength of samples printed

Table 2 Printing parameter description

Printing Parameter	Definition of the parameter
Bed Temperature (°C)	Temperature of the print bed during printing process [119].
Flow Rate (% or mm/s)	Rate at which the printer will extrude material during printing [120].
Infill Density (%)	Percentage measurement how much filament will be printed inside the shell [49].
Infill Pattern	Structure/ Shape that is printing inside the part at the set density [121].
Infill Overlap (%)	Parts of the infill walls that overlap which is typically attributed to infill densities over 100% [122].
Layer Height (mm)	Adjusts the height each layer of filament is printed at [123].
Nozzle Diameter (mm)	Exit diameter of the print nozzle [119].
Nozzle Temperature (°C)	Temperature of the print head nozzle during printing [124].
Oversizing factors (%)	Part increase percentages for shrinkage compensation [125].
Print Orientation (Flat, Flipped, Vertical)	Orientation of the part relative to the print bed [126]. The print orientation discussed in the further printing sections has been modified to keep all wording consistent as detailed below.
	
Print Speed (mm/s)	Speed at which the printing head travels during printing [127].
Raster Angle (°)	Angle of the deposition tool path with respect to the x-axis [128].
Shell Thickness (mm)	The thickness of the contour lines used to cover the infill structure [129].

with various infill densities and the effect of print orientation on tensile strength. Results found that increased infill densities increased the compression strength and decreased the compressive stress at comparable levels. In terms of the printing orientation effect, samples printed flat had the highest ultimate tensile strength (UTS) with 311.81 MPa. Similar results on the effect of infill densities were found by Wang et al. [42]. Schmacher and Moritzer [86] investigated different infill patterns on FDMm 316L SS and found that using a rectilinear pattern provided better tensile strengths compared to a honeycomb pattern. Atatreh et al. [93] also reported that FDMm printed 17-4PH SS with solid infill patterns such as rectangular provided better UTS compared to honeycomb infill patterns.

Hassan et al. [64] tested the effects of layer height and flow rate on the porosity and grain size of FDMm printed 316L SS. Study concluded that an increase in flow rate led to additional porosity and larger grain size while an increase in layer height yielded no effect on the porosity or grain size. Kurose et al. [63] investigated the effects of printing layer heights and printing orientation on the relative density of FDMm printed 316L SS. It was concluded that print orientation didn't have a significant impact on relative density; however, the samples printed flat had the highest tensile strength. Similarly, Suwanpreecha and Manonukul [100] found that

samples printed using a flat orientation had a higher flexural strength. Obadimu et al. [87] tested the effects that layer height, raster angle, and print speed have on the mechanical properties of 316L SS printed samples. It was revealed that layer height and raster angle significantly influenced the UTS while print speed does not show any statistical effect. Caminero et al. [68] examined the effects of nozzle size, print speed and print orientation. The densest sample were printed using parameters 0.20 mm layer height, 30 mm/s flow rate, and flat orientation. Parenti et al. [69] found that a 10 mm/s flow rate and a nozzle temperature of 120–125°C provided the best samples. Moritzer et al. [72] found that using a 0.40 mm nozzle diameter and an infill density of 120% is the optimal level of printing parameters. It was also noted that minimizing the layer height provided better first layer application.

Furthermore, Abe et al. [75] examined the effect of print orientation on the UTS of FDM printed 17-4PH SS. A flat orientation provided the best UTS followed by flipped and then vertical. Alkindi et al. [95] reported similar results when testing intermediate printing orientations between flat and vertical orientations. Godec et al. [77] examined the effects of nozzle temperature, flow rate multiplier and layer thickness had on FDM printed 17-4PH SS. It was concluded that an increased nozzle temperature and flow rate

Table 3 Literature studies FDMm printing information

Study	Printing parameters tested	Study results
Quarto et al. [61] (316L SS)	<ul style="list-style-type: none"> • Infill Pattern (Line, Wall) • Layer height (0.10, 0.40 mm) • Nozzle Temperature (179, 240°C) • Print speed (20, 50 mm/s) 	<p>Nozzle temperature decrease from 240 to 179°C showed no change in shrinkage or porosity. Print speed increase from 20 to 50 mm/s led to an increase in porosity and shrinkage. A layer height increase from 0.1 to 0.4 mm decreased the shrinkage. The best sample density obtained using 20 mm/s print speed, 0.1 mm layer height and line infill pattern.</p>
Ait-Mansour et al. [85] (316L SS)	<ul style="list-style-type: none"> • Bed Temperature (90°C) • Infill Density (25, 50, 75, 100, 125%) • Layer Height (0.20 mm) • Nozzle Temperature (235°C) • Print Speed (30 mm/s) 	<p>Print infill density was tested from 25 to 125% using 25% increments. Samples with infill densities 50–125% had similar compressive strengths, however, the compressive stress increased as the infill density decreased. The 25% infill density samples showed significantly lower compressive strengths. Tensile strength for vertical, flipped and flat printing orientation were tested. Flat printed samples (311.81 MPa) had significantly higher tensile strength compared to the vertical (218.72 MPa) and flipped (229.58 MPa) orientation.</p>
Schumacher and Moritzer [86] (316L SS)	<ul style="list-style-type: none"> • Bed Temperature (100, 120°C) • Infill Density (5, 30, 60, 90%) • Infill Pattern (Rectilinear, Honeycomb) • Layer Height (0.15, 0.20 mm) • Nozzle Diameter (0.4 mm) • Nozzle Temperature (230, 240°C) 	<p>Infill densities were increased from 5% to 30, 60 and 90% using rectilinear and honeycomb infill pattern. The tensile strength increased as the infill density increased. Rectilinear infill pattern achieved consistently higher tensile strength compared to honeycomb infill pattern.</p>
Kurose et al. [63] (316L SS)	<ul style="list-style-type: none"> • Bed Temperature (70°C) • Infill Density (100%) • Layer Height (0.10, 0.30 mm) • Nozzle Diameter (0.4 mm) • Nozzle Temperature (170°C) • Printing Orientation (Variable with coordinate axes) • Printing Speed (10 mm/min) • Shell Thickness (0.80 mm) 	<p>The highest tensile strength of 522 MPa with 50% elongation at break occurred at 90% infill density and rectilinear infill pattern. Two different layer heights (0.1 mm, 0.3 mm) were examined with flat, flipped and vertical printing orientations. A layer height of 0.1 mm had the highest average relative density across all orientations. Flat specimens had the highest tensile stress followed by flipped then vertical specimens. Printed specimens using a flat orientation with a layer height of 0.1 mm had the highest tensile strength of 453 MPa.</p>
Hassan et al. [64] (316L SS)	<ul style="list-style-type: none"> • Flow rate (7.5, 12.5, 17.5 mm/s) • Infill Pattern (Rectangular) • Layer Height (0.30, 0.40, 0.50 mm) • Print Orientation (Horizontal, Vertical) • Nozzle Diameter (0.8 mm) • Nozzle Temperature (135°C) • Raster Angle (45°) 	<p>An ANOVA examination was conducted showing the effects that printing parameters had on the final sintered properties. A layer height change from 0.30 to 0.40 mm and 0.50 mm proved no effect on the porosity and grain size of the samples. A flow rate increase from 7.5 to 12.5 mm/s and 17.5 mm/s increased the porosity and grain size observed in the samples.</p>
Obadimu et al. [87] (316L SS)	<ul style="list-style-type: none"> • Layer Height (0.15, 0.20, 0.25 mm) • Nozzle Diameter (0.4 mm) • Print Speed (30, 35, 40 mm/s) • Raster Angle (+45/−45/0/90°) 	<p>An ANOVA table showed an increase in print speed from 30 to 35 and 40 mm/s show no significant impact on the ultimate tensile strength. Raster angle and layer height showed significant statistical influence on the UTS. The printing combination of 0.20 mm layer height and +45/−45° had the highest UTS of 450.3 MPa.</p>

Table 3 (continued)

Study	Printing parameters tested	Study results
Camirero et al. [68] (316LX SS)	<ul style="list-style-type: none"> • Bed Temperature (100°C) • Flow Rate (30, 40, 50 mm/s) • Infill Density (100%) • Infill Pattern (Concentric) • Layer Height (0.20, 0.25 mm) • Nozzle Diameter (0.4, 0.6 mm) • Nozzle Temperature (230°C) • Print Orientation (Flat, Flipped, Vertical) 	<p>The 0.6 mm nozzle size proved to provide less shrinkage as there was less interlayer porosity. A flat orientation had the lowest surface roughness compared to the other printing orientations. The densest sample was created using a 0.6 mm nozzle, 0.20 mm layer height and a feed rate of 30 mm/s. The authors note that this combination created better compacting of the deposited filament and layers. However, these printing parameters had worse dimensional accuracy compared to the small nozzle diameter with a higher feed rate.</p>
Parenti et al. [69] (316L SS)	<ul style="list-style-type: none"> • Flow Rate (10 mm/s) • Nozzle Diameter (0.9 mm) • Nozzle Temperature (90–140°C) • Raster Angle (+45°/–45°) 	<p>The authors found that using a flow rate of 10 mm/s and a nozzle temperature of 120–125°C gave the best results from green part milling procedure.</p>
Moritzer et al. [72] (316L SS)	<ul style="list-style-type: none"> • Bed Temperature (120°C) • Infill Density (87.5, 120, 152.2%) • Infill Pattern (Rectilinear) • Layer Height (0.125 mm) • Nozzle Diameter (0.25, 0.40 mm) • Print Speed (20, 25, 34 mm/s) • Raster Angle (45°/90°) 	<p>A decreased layer height had better first layer adhesion. A larger nozzle size of 0.40 mm and an infill density of 120% was recommended for printing. Printed parts were printed to be 99% dense. Sintered parts had a UTS of 520 MPa.</p>
Kedziora et al. [88] (316L SS)	<ul style="list-style-type: none"> • Bed Temperature (100°C) Infill Density (100%) Layer Height (0.15 mm) Nozzle Diameter (0.4 mm) Nozzle Temperature (250°C) Oversizing Factors: X, Y, Z, % (21.35, 21.35, 26) 	<p>Bed Temperature (100°C) Infill Density (100%) Layer Height (0.15 mm) Nozzle Diameter (0.4 mm) Nozzle Temperature (250°C) </p>
Santamaria et al. [89] (316L SS)	<ul style="list-style-type: none"> • Bed Temperature (65°C) Layer Height (0.15 mm) Nozzle Diameter (0.40 mm) Nozzle Temperature (175°C) Print Speed (30 mm/s) Raster Angle (+45°/–45°) Shell Thickness (1.5 mm) 	<p>Bed Temperature (65°C) Layer Height (0.15 mm) Nozzle Diameter (0.40 mm) Nozzle Temperature (175°C) Print Speed (30 mm/s) </p>
Gong et al. [90] (316L SS)	<ul style="list-style-type: none"> • Layer Height (0.20 mm) Nozzle Temperature (235°C) Print Speed (60 mm/s) 	<p>Layer Height (0.20 mm) Nozzle Temperature (235°C) Print Speed (60 mm/s)</p>
Damon et al. [65] (316L SS)	<ul style="list-style-type: none"> • Bed Temperature (120°C) Flow Rate (100%) Infill Pattern (Parallel lines) Layer Height (0.48 mm) Nozzle Temperature (210°C) Printing Speed (2000 mm/min) Raster Angle (+45°/–45°) 	<p>Bed Temperature (120°C) Flow Rate (100%) Infill Pattern (Parallel lines) Layer Height (0.48 mm) Nozzle Temperature (210°C) </p>
Tosto et al. [91] (316L SS)	<ul style="list-style-type: none"> • Bed Temperature (90°C) Infill Density (100%) Layer Height (0.14 mm) Nozzle Diameter (0.4 mm) Nozzle Temperature (240°C) 	<p>Bed Temperature (90°C) Infill Density (100%) Layer Height (0.14 mm) Nozzle Diameter (0.4 mm) Nozzle Temperature (240°C)</p>
Liu et al. [60] (316L SS)	<ul style="list-style-type: none"> • Infill Pattern (Rectangular) Layer Height (0.20 mm) Nozzle Temperature (230°C) 	<p>Infill Pattern (Rectangular) Layer Height (0.20 mm) Nozzle Temperature (230°C)</p>
Thompson et al. [66] (316L SS)	<ul style="list-style-type: none"> • Flow Rate (105%) Infill Density (100%) Infill Pattern (Rectangular) Nozzle Diameter (0.6 mm) Nozzle Temperature (270–290°C) Raster Angle (+45°/–45°) 	<p>Flow Rate (105%) Infill Density (100%) Infill Pattern (Rectangular) Nozzle Diameter (0.6 mm) Nozzle Temperature (270–290°C) </p>
Sadaf et al. [62] (316L SS)	<ul style="list-style-type: none"> • Bed Temperature (60°C) Infill Density (100%) Infill Pattern (Rectangular) Layer Height (0.20 mm) Nozzle Diameter (0.6 mm) Nozzle Temperature (220°C) Printing Speed (80 mm/s) Raster Angle (0–90°) 	<p>Bed Temperature (60°C) Infill Density (100%) Infill Pattern (Rectangular) Layer Height (0.20 mm) Nozzle Diameter (0.6 mm) </p>
Moussapour et al. [35] (316L SS)	<ul style="list-style-type: none"> • Bed Temperature (60°C) Infill Density (100%) Layer Height (0.20 mm) Nozzle Temperature (210°C) Printing Speed (15 mm/s) 	<p>Bed Temperature (60°C) Infill Density (100%) Layer Height (0.20 mm) Nozzle Temperature (210°C) Printing Speed (15 mm/s)</p>
Wagner et al. [67] (316L SS)	<ul style="list-style-type: none"> • Bed Temperature (60°C) Flow Rate (100%) Infill Density (100%) Infill Pattern (Rectangular) Layer height (0.16 mm) Nozzle Diameter (0.25 mm) Nozzle Temperature (230°C) Print Orientation (Flat) Print Speed (280 mm/min) 	<p>Bed Temperature (60°C) Flow Rate (100%) Infill Density (100%) Infill Pattern (Rectangular) Layer height (0.16 mm) Nozzle Diameter (0.25 mm) Nozzle Temperature (230°C) Print Orientation (Flat) Print Speed (280 mm/min)</p>

Table 3 (continued)

Study	Printing parameters tested	Study results
Wang et al. [42] (316L SS)	Infill Density (100%) Infill Pattern (Zig-Zag) Layer Thickness (0.20 mm) Nozzle Diameter (0.5 mm) Nozzle Temperature (230°C) Print Speed (30 mm/s)	
Ortega et al. [71] (316L SS)	Bed Temperature (Room Temperature) Layer Height (0.15 mm) Nozzle Temperature (170°C) Print Speed (40 mm/s)	
Jimbo and Tateno. [92] (316L SS)	Layer Height (0.22 mm) Nozzle Diameter (0.4 mm) Nozzle Temperature (240°C)	
Burkhardt et al. [74] (316L SS)	Nozzle Diameter (0.5 mm) Print Speed (50 mm/s)	
Abe et al. [75] (17-4PH SS)	<ul style="list-style-type: none"> • Infill Density (100%) • Infill Pattern (Rectangular) • Layer Height (0.1 mm) • Print Orientation (Flat, Flipped, Vertical) • Raster angle (+45°/−45°) 	The flat specimen orientation had the lowest number of pores in the microstructure analysis and the best ultimate tensile strength compared to other orientations.
Godec et al. [77] (17-4PH SS)	<ul style="list-style-type: none"> • Bed Temperature (100°C) • Flow Rate (95, 101, 110, 120, 127%) • Infill Density (100%) • Infill Pattern (Rectangular) • Infill Overlap (15%) • Layer Thickness (0.12, 0.15, 0.20, 0.25, 0.28 mm) • Nozzle Temperature (210, 220, 235, 250, 260°C) • Printing Speed (35 mm/s) • Raster Angle (45°) 	Visual inspection after printing showed that an increase in nozzle temperature and flow rate resulted in a visibly smoother sample. A nozzle temperature of 235°C, flow rate multiplier of 127% and layer thickness of 0.2 mm achieved the best tensile properties of all the as-printed parts. An ANOVA table showed that nozzle temperature, as well as an increased flow rate multiplier and layer thickness had significant effects on the as-printed tensile properties.
Atatreh et al. [93] (17-4PH SS)	<ul style="list-style-type: none"> • Infill Pattern (Solid, Triangular) • Layer Height (0.125, 0.129 mm) 	Triangular infill samples had significantly lower tensile strength compared to the solid printed samples. The authors also noted a fracture zone occurring at the triangles tip to tip connection point.
Lavecchia et al. [94] (17-4PH SS Markforged)*	<ul style="list-style-type: none"> • Infill Density (100%) • Nozzle Diameter (0.4 mm) • Print Orientation (Flat, Vertical) • Raster Angle (+45°/−45°) • Bed Temperature (130°C) • Flow Rate (104%) • Infill Density (100%) • Nozzle Diameter (0.4 mm) • Nozzle Temperature (245°C) • Print Speed (35 mm/s) • Print Orientation (Flat, Vertical) 	Comparison between 2 and 6 wall layers with vertical and flat build orientations. The best UTS was found with 2 wall layers using a flat orientation. Slight deviations in UTS are noted between the 2 and 6 wall layers. Print orientation had a significant effect on the samples UTS.
Lavecchia et al. [94] (17-4PH SS BASF Ultrafuse)*	<ul style="list-style-type: none"> • Bed Temperature (130°C) • Flow Rate (104%) • Infill Density (100%) • Nozzle Diameter (0.4 mm) • Nozzle Temperature (245°C) • Print Speed (35 mm/s) • Print Orientation (Flat, Vertical) 	As the print orientation was increased from 0 to 90° the tensile stress and elongation at break steadily decreased until ≈60°. At 0° and 10° orientation, the tensile strength was 947.26 and 949.87 MPa, respectively
Alkindi et al. [95] (17-4PH SS)	<ul style="list-style-type: none"> • Infill density (100% Infill) • Layer Height (0.125 mm) • Print Orientation (Flat to vertical using 10° intervals) • Shell Thickness (1 mm) 	
Lawrence et al. [96] (17-4PH SS)	<ul style="list-style-type: none"> • Infill Density (37, 100%) • Infill Pattern (Lines, Triangle) • Raster Angle (+45°/−45°) 	Solid infill specimens achieved an UTS close to wrought 17-4PH while the triangular infill patterns UTS was significantly lower. Triangular infill pattern had a higher defect percentage than the solid infill pattern specimens.

Table 3 (continued)

Study	Printing parameters tested	Study results
Henry et al. [97] (17-4PH SS)	<ul style="list-style-type: none"> • Oversizing Factors: X, Y, Z, % (20, 20, 20) • Print Orientation (Flat, Flipped, Vertical) • Raster Angle (+45°/−45°, 0°/90°) 	<p>Samples with a flipped orientation and infill lines parallel to the pull direction achieved higher UTS compared to samples with −45°/+45° raster angle.</p>
Bjorheim and La Torrance Lopez [98] (17-4 PH SS)	<ul style="list-style-type: none"> • Print Orientation (Flat, Flipped, Vertical) • Raster Angle (+45°/−45°) 	<p>Samples printed flat achieved an average UTS of 1070 MPa which was significantly higher than the average UTS of the flipped and vertical orientations (814 and 726 MPa, respectively).</p>
Fongsamootr et al. [99] (17-4PH SS)	<ul style="list-style-type: none"> • Infill Density (16, 20, 24, 100%) • Infill Pattern (Triangle, Solid) • Raster Angle (0°/60°, 15°/45°/75°, 30°/90°) 	<p>UTS increased as the infill density increased. A full dense sample was 6.3X higher UTS compared to 16% dense specimen. Raster angle of 0°/60° achieved the highest Ultimate strength compared to the other Raster angles tested.</p>
Suwanpreecha and Manomukul [100] (17-4PH SS)	<ul style="list-style-type: none"> • Bed Temperature (70°C) • Infill Density (100%) • Layer Height (0.125 mm) • Nozzle Temperature (220°C) • Printing Orientation (Flat, Flipped, Vertical) • Printing Speed (20 mm/s) • Raster Angle (+45°/−45°) 	<p>Samples that were printed Flat and Flipped had a higher as-printed and relative sintered densities compared to a vertical print orientation. Flat printed samples achieved the highest Flexural strength compared to the other orientations.</p>
Kendziora et al. [88] (17-4PH SS)	<p>Bed Temperature (115°C) Infill Density (100%) Layer Height (0.125 mm) Nozzle Diameter (0.45 mm) Nozzle Temperature (220°C) Oversizing Factors: X, Y, Z, % (19.5, 19.5, 20)</p>	
Jiang and Ning [79] (17-4PH SS)	<p>Infill Density (100%) Layer Height (0.05 mm) Nozzle Diameter (0.4 mm)</p>	
Watson et al. [76] (17-4 PH SS)	<p>Layer Height (0.05 mm) Nozzle Diameter (0.4 mm)</p>	
Bouaziz et al. [101] (17-4 PH SS)	<p>Infill Density (100%) Layer Height (0.05 mm) Print Orientation (Flat) Raster Angle (+45°/−45°)</p>	
Chemkhi et al. [102] (17-4 PH SS)	<p>Infill Density (100%) Layer Height (0.05mm) Nozzle Temperature (218°C)</p>	
Galati and Minetola [103] (17-4 PH SS)	<p>Infill Pattern (Solid, Closed Triangle) Layer Height (0.125, 0.05 mm)</p>	
Forcelllese et al. [104] (17-4 PH SS)	<p>Nozzle Diameter (0.4 mm) Print Orientation (0°, 45°, 90°)</p>	
Watson et al. [105] (17-4PH SS)	<p>Layer Height (0.05 mm) Nozzle Temperature (0.4 mm) Oversizing Factors: X, Y, Z, % (18.6, 18.6, 19.5)</p>	
Rahimi and Zamani [82] (4605 Steel)	<p>Bed Temperature (90°C) Layer Height (0.2 mm) Nozzle Temperature (170°C) Print Speed (30 mm/s) Shell Thickness (1 mm)</p>	
Vetter et al. [83] (1.2083 Tool Steel)	<ul style="list-style-type: none"> • Bed Temperature (60°C) • Flow Rate (150%) • Infill Pattern (Line) • Layer Height (0.05 mm) • Nozzle Diameter (0.4 mm) • Nozzle Temperature (140°C) • Printing speed (20/25, 60/80 mm/s) 	<p>Elevating the print speed from 20/25 to 60/80 mm/s decreased the as-printed density from 4.95 to 4.82 g/cm³. The authors noted that this is probably due to increased filament slip while printing. Increasing the flow rate from 150 to 160% resulted in the highest print density of 5.11 g/cm³. An increase in printing temperature from 120 to 145°C provided insignificant change in print density.</p>
Charpentier et al. [84] (High Carbon Tool Steel)	<p>Bed Temperature (60°C) Infill Density (100%) Layer Height (0.30 mm) Nozzle Diameter (0.8 mm) Nozzle Temperature (200°C)</p>	

*Printer manufacturers were specified as each printer used different printing parameters

resulted in a visible smoother sample. An increased flow rate multiplier resulted in a strand overlap increase from 97 to 127%. The authors noted an increase in nozzle temperature, flow rate multiplier and layer thickness improved the tensile strength of the sample. Lavecchia et al. [94] reported that the highest UTS occurred with less shell thickness and a flat orientation. Lawrence et al. [96] concluded that solid infill pattern had significantly higher UTS compared to triangular infill pattern. This was further confirmed by Fong-smootr et al. [99]. Henry et al. [97] found that samples with a flipped orientation with infill lines parallel with the tensile pull direction achieved the best UTS.

Vetter et al. [83] examined the effects of printing parameters on FDM printed 1.2083 tool steel. Results concluded that an increase in flow rate increased the printed density while an increase in print speed decreased the printed density. A change in nozzle temperature provided no significant change to the print density.

3 Debinding process

The debinding process removes the thermoplastic binder from the print in preparation for sintering. A good binder will contain the metallic powder well, prevent warping of the printed part and debind without difficulty [55]. There are four major types of debinding processes: thermal, solvent, water, and catalytic debinding [70]. Thermal debinding removes the binder through vaporizing/evaporating the binder within the part [106]. Solvent debinding removes a portion of the binder (typically wax based) by dissolving it in a solvent [106, 107]. Some binders can also be dissolved using agitated warm water. Catalytic debinding breaks down the binder by reacting with the binder and changing it to gas and exhausting it out of the system [106].

Debinding time and temperature are dependent on type of binder used in the filament [55]. A rapid increase in temperature can result in violent thermal expansion during

vaporization/evaporation of the polymer. The escaping gas can cause increased porosity and large defects within the printed part [21]. Many studies only note that a debinding process had been completed, without focusing on the debinding process parameters. The goal of this section is to report debinding processes used to remove the binder material in high melt iron alloys. The debinding temperature cycle is a critical part of the debinding process. Many literatures have studied the debinding process in FDM 3D printing. Lu [37] examined the thermal degradation temperature of different filaments from The Virtual Foundry. The thermal degrading of 316L SS filament started at 227.33 and 252.08°C and was fully degraded around 416°C with a final weight percentage around 83%. The High Carbon filament started degrading at 267.83 and 262.95°C and was fully degraded around 421°C with a final weight percentage around 76%.

Mousapour et al. [35] used microscopy analysis to investigate the effects of debinding rates on the porosity of 316L SS printed using FDM. Printed samples were heated to 250°C at a rate of 5°C/min then up to 400°C using a rate of 0.2, 0.7, and 1°C/min. The process was monitored until no further mass changes were recorded. The parts were subsequently sintered for sintered porosity analysis. Samples of each debinding rate were tested at a sintering temperature of 1360°C for 6 h. Sintered samples with lower debinding rates had a higher relative density. The results showed a substantial porosity improvement as the debinding rate decreased (see Fig. 3).

Thompson et al. [66] research into the effects of debinding rates agreed that lower debinding rate reduced the porosity. External visible defects at different debinding rates can be seen in Fig. 4.

Wagner et al. [67] examined how parts of the debinding cycle affected the removal of the binder. It was concluded that the two-step debinding process of solvent and thermal debinding effectively removed the binder. Complete thermal degradation of the stearic acid portion of the binder took place between 160 and 260°C while the thermal decomposition of TPE took place between 300 and 460°C.

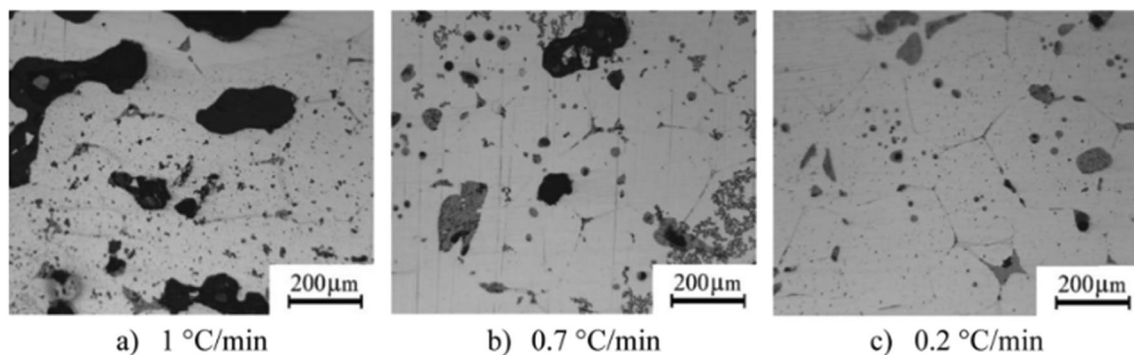


Fig. 3 Porosity comparison in microstructure for debinding rates of (a) 1°C/min (b) 0.7°C/min (c) 0.2°C/min done by Mousapour et al. [35]

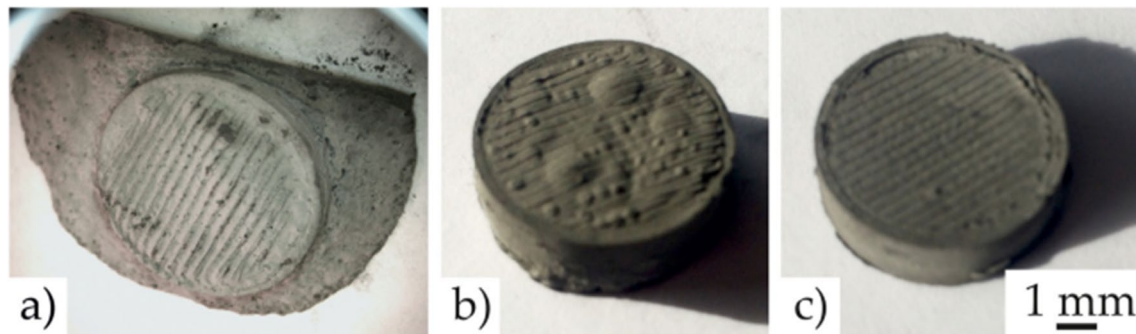


Fig. 4 Visible thermal defects from debinding rates of (a) 3°C/min, (b) 1°C/min, and (c) 0.2°C/min [66]

Investigation into the effects of the heating rate on the microstructure revealed that the binder content has a large effect in the formation of defects within the sample. Samples with 23% binder using a heating rate of 5°C/min showed open blisters on the surface after sintering whereas no blisters were noted at a heating rate of 0.5°C/min. After using 99.5% Acetone as a solvent debinder, microscopic images of the remaining primary and secondary binder were taken by Ortega Varela de Seijas et al. [71] (see Fig. 5).

The debinding information provided in literary studies for FDMm printing are reported in Table 4.

4 Sintering process

Most the FDMm printed high melt iron alloys undergo a similar sintering process with alterations to the temperatures and hold times. To start the sintering process, the kiln temperature is slowly raised from room temperature through the thermal debinding process if applicable. The temperature is subsequently raised to a sub-sinter temperature allowing the center of the crucible rise to the kiln temperature. Finally, the temperature is raised to the sintering temperature, this is where the metallic powder fuses together to create the final metal part. The sintering time is another major parameter that can be optimized. Some studies use a lower temperature for a longer amount of time, while other choose a higher

temperature with a shorter sinter cycle. Key mechanical properties such as shrinkage, porosity, and microstructure can be greatly affected by the applied sintering cycles.

Sintering and heat treatment are the final steps to having a complete FDMm printed part. The sintering process fuses the metallic powder from the filament into one solid metal piece. Temperature ramp rates, sintering temperature and sintering hold time are the major contributing factors to the successfulness of the finished print. FDMm filament supplier such as The Virtual Foundry recommends setting the sintering temperature between 80 and 90% of the metals melting temperature [40]. This would result in 316L SS and 17-4PH SS having a sinter temperature between 1200 and 1350°C [110, 111]. Heat treatment processes can be applied to the samples to enhance their microstructure and mechanical properties. The furnace is cooled to room temperature for removal of the completed FDMm parts. Experimental mechanical analysis such as microstructure analysis, spectroscopy study, and tensile testing can help researchers to establish the effects of printing parameters and post printing techniques.

Shrinkage and porosity of the final part are major downsides in the FDMm printing quality, the removal of a high-volume binder creates significant porosity within the print before sintering [55]. During the sintering process the printed part shrinks to fill the porosity left in the binder's wake. Sintering processes attempt to establish low/controllable shrinkage while maintaining low porosity. In the FDMm

Fig. 5 Micrograph of the primary and secondary binder [71]

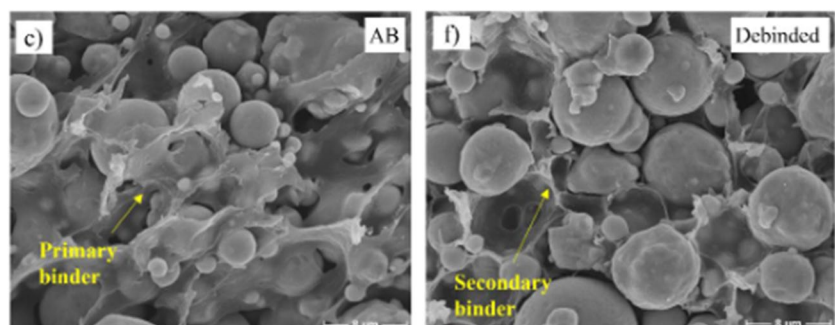


Table 4 Literature studies FDMm debinding information

Study	Debinding process
Mousapour et al. [35]	Thermal debinding was completed at 400°C for 1 h with different ramp rates until a specific mass loss was observed.
Abe et al. [75]	Thermal debinding was completed at 600°C under nitrogen gas for 2 h.
Liu et al. [60]	Thermal debinding was completed at 120°C under nitrogen gas for 8 h.
Lu et al. [37]	Thermal debinding was completed at 300°C.
Quarto et al. [61]	Catalytic debinding was preformed at 120°C until insufficient mass loss occurred.
Damon et al. [65]	Catalytic debinding using Acidic gas at 120°C for 2 h followed by thermal debinding at 600°C for 1 h to burn away residual binder.
Sadaf et al. [62]	Thermal debinding was preformed under Hydrogen gas at 500°C for 1.5 h.
Gonzalez-Gutierrez et al. [78]	Solvent debinding was done using a cyclohexane solvent at 70°C until a mass loss of 5.9% was achieved.
Thompson et al. [66]	Solvent debinding was completed using a cyclohexane solvent at 65°C for 24–57 h until a 1% mass loss was completed. This was followed by a thermal debinding in a vacuum furnace between 375 and 500°C.
Kurose et al. [63]	Thermal debinding was completed under nitrogen gas at 600°C for 2 h.
Watson et al. [76]	Part is initially debound in an organic solvent for 30–40 h. This is followed by a thermal debinding process at 400°C in an argon/hydrogen rich environment to remove the remainder of the binder.
Hassan et al. [64]	For initial debinding the print was put in 40°C solvent for 48 h. Following solvent debinding, the parts were added to a kiln Slow heating to remove moisture from the part with thermal debinding being completed at 300°C for 2 h.
Wagner et al. [67]	Solvent debinding in cyclohexane for 7 h at 60°C followed by thermal debinding at 490°C for 10 h
Vetter et al. [83]	Solvent debinding in acetone at 42.5°C with all soluble binder removed from samples <12 mm between 30 and 40 h. Insoluble binder was thermally removed between 300 and 400°C.
Atatreh et al. [93]	Solvent debinding wash until specified mass loss is achieved.
Wang et al. [42]	Thermal debinding of binder through heating to 200°C at a rate of 5 °C/s with a hold time of 2 h. The temperature was increased to 425°C and held for 1 h.
Camirero et al. [68]	Catalytic debinding in nitric acid gas at 120°C with a rate of 1–2 mm/h for each external surface. This was followed by thermal debinding at 600°C for 1 h with a ramp of 5°C/min for 1 h.
Lavecchia et al. [94] (2 Different Debinding Processes)	Solvent debinding in the industrial solvent Opteon SF79. Solvent was kept at 50°C until a mass loss condition was reached. Thermal debinding was completed in the sintering process for the remaining binder.
Pellegrini et al. [80] (2 Different Debinding Processes)	Catalytic debinding in nitric acid at 120°C until a mass loss condition was reached. Solvent debinding in the industrial solvent Opteon SF79 at 50°C until a mass loss condition was reached.
Santamaria et al. [89]	Catalytic debinding at 120°C for 8 h in a HNO ₃ environment
Rahimi and Zamani [82]	Solvent debinding at 50°C for 15 h followed by thermal debinding at 550°C for 2 h
Parenti et al. [69]	Solvent debinding completed in a n-heptane solution at 70°C for 5 h followed by thermal debinding
Ortega Varela de Seijas et al. [71]	Printed were submerged in 50°C stirred water followed by a thermal debinding at 680 for 10 h.
Lawrence et al. [96]	Solvent debinding using acetone solvent with 99.5% purity at 45°C until no further mass loss was recorded after 24 h.
Henry et al. [97]	Solvent debinding in industrial solvent Opteon SF79 until a mass loss condition is met.
Ghadimi et al. [108]	Solvent debinding in industrial solvent Opteon SF79 for a minimum of 6 h until a mass loss condition is met.
Chemkhi et al. [102]	Solvent debinding in a heated industrial solvent Opteon sion until a mass loss condition is met.
Galati and Minetola [103]	Solvent debinding in industrial solvent Opteon SF79 for 12 h.
Forcellese et al. [104]	Solvent debinding in a heated industrial solvent Opteon sion for a minimum of 28 h
	Solvent debinding using trans-1,2 dichloroethylene for 30–40 h.

Table 4 (continued)

Study	Debinding process
Watson et al. [105]	Debinding between 30 and 40 h until a mass loss condition is met followed by thermal debinding at 400°C.
Charpentier et al. [84]	Thermal debinding carried out in a neutral nitrogen rich environment starting at 25 to 300°C at a rate of 30°C/h
Gonzalez-Gutierrez et al. [73]	Solvent debinding in Cyclohexane at 75°C for 12 h until a mass loss condition is met
Giberi et al. [109]	Water debinding at 60°C for 10 h
Sumanprecha and Manonukul [100]	Thermal debinding at 450°C for 100 min.

process, the x-y direction shrinkage is typically uniform; however, the z-direction shrinkage is increased due to the effect of gravity [63]. Mechanical properties analysis such as tensile or compressive test provides insight into the successfulness of process parameters and a comparison point for metal FDMm.

This section provides information into the key sintering parameters and microstructure studies on sintered FDMm high melt iron alloy parts. Listed below in literary work into the heat treatment and microstructure analysis of FDMm printed and sintered high melt iron alloy parts.

Table 6 displays information of the sintering processes, mechanical testing results and mechanical properties for FDM printed 316L SS and 17-4PH SS. For comparison, 316L SS has a UTS of 518 MPa with a density of 8 g/cc and 17-4 PH SS had a UTS of 1379 MPa with a density of 7.8 g/cc [111, 115–117].

4.1 Microstructure analysis

Microstructure imaging can provide vital incite into how process changes are affecting the parts internally. Since the microstructure is primarily created during the sintering phase. Studies with unique microstructures and their associated sintering parameters are described below. Finally, this section discusses heat treatment after sintering and Surface Mechanical Attrition Treatment (SMAT) to improve mechanical properties and alter microstructure.

Microscopic evaluation of sintered FDMm printed 316L SS preformed by Mousapour et al. [35]. This work compared the microstructure at the top to the bottom of the sample after sintering (see Fig. 6). In this work, samples were sintered with a peak sintering temperature of 1360°C with a 6-h dwell time. The top of the sample contained more porosity than the bottom due to densification of gravity.

Liu et al. [60] performed microstructure analysis for FDMm printed 316L SS sintered at a peak sinter temperature of 1360°C for 2 h (see Fig. 7). The finding revealed that the printing layer lines were still evident in the fully sintered 316L SS part. The authors also highlighted a twin crystal formation as seen in Fig. 8 that occurred in FDM printed 316L SS. The twin crystal microstructure noted in Fig. 8

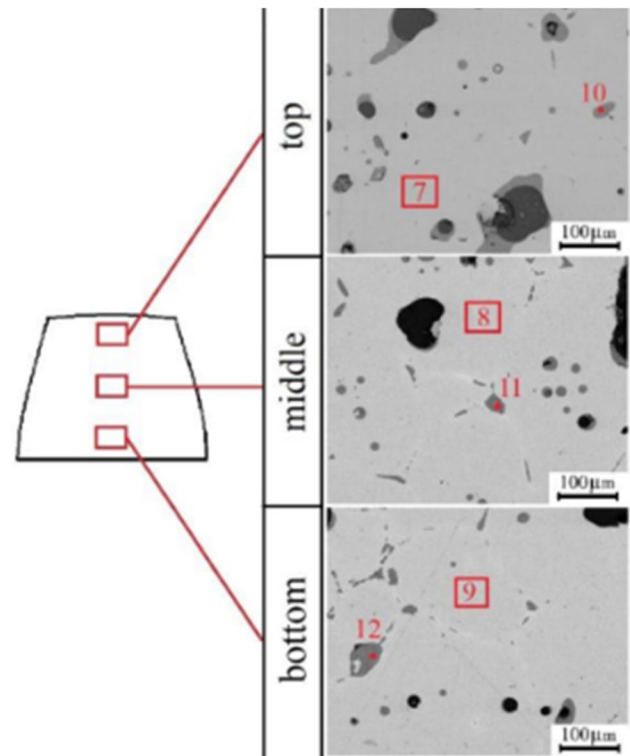


Fig. 6 316L SS microstructure at 100 μm [35]

increases the hardness of the specimen. Similar layer lines were found by Atatreh et al. [93], Ghamdimi et al. [108], and Kedziora et al. [88] using FDMm printed 316L SS and 17-4PH SS.

Kurose et al. [63] investigated the fracture surfaces of 316L SS samples sintered using a peak sinter temperature of 1280°C held for 2 h. Layer directions going parallel to the force application achieved high tensile strength and had similar break structures as seen in Fig. 9(a) and (b). The samples with layer directions going to the force application had a different fracture surface and significantly lower tensile strength results as seen in Fig. 9(c) [63]. The author notes that “the voids oriented perpendicular to the tensile direction in the L-specimen would act as defects which could cause stress concentrations” [63].

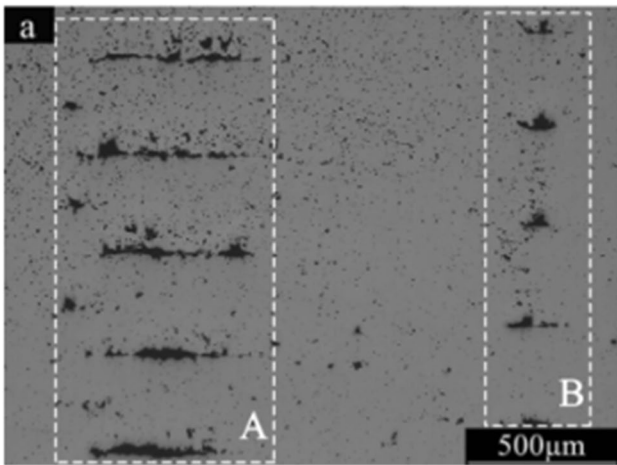


Fig. 7 Sintered 316L SS imaging with layer lines visible (A), (B) [60]

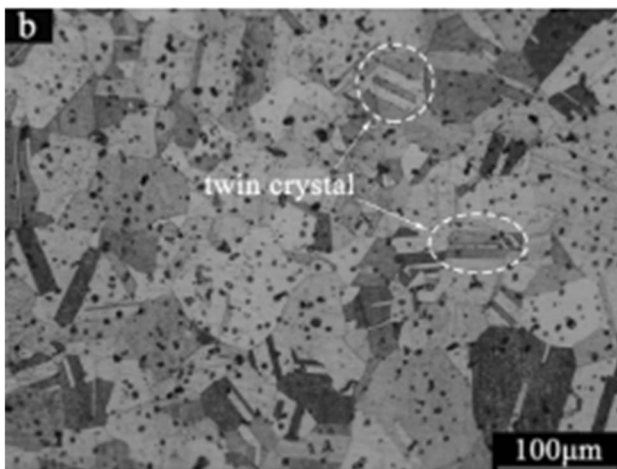
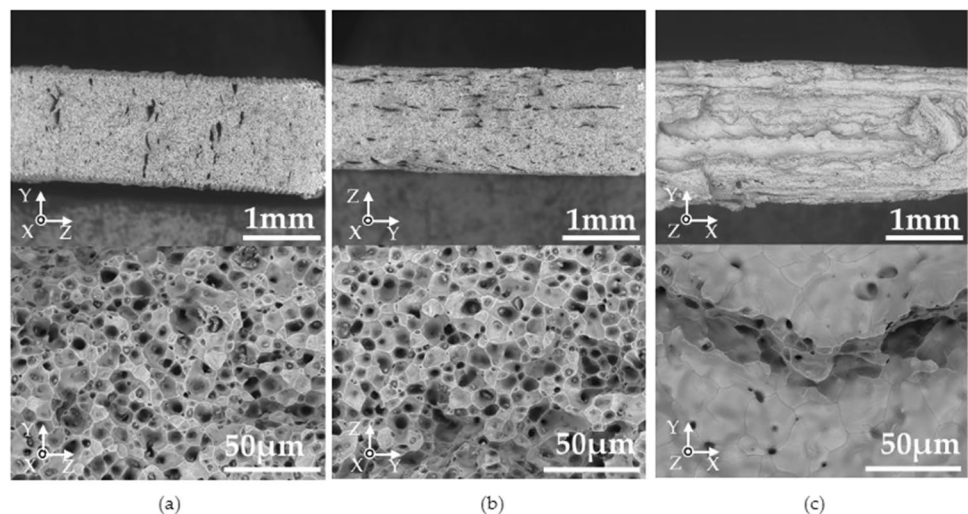


Fig. 8 316L SS microstructure at 100 μm [60]

Fig. 9 Fracture surfaces of tensile samples at each printing orientation showing internal printing porosity at (a) flat (b) flipped (c) vertical [63]



As noted in a previous work, layer lines and large porosity were evident after sintering at 1280 and 1360°C for 2 h dwell. In addition, Wagner et al. [67] used micrography to examine the porosity at different peak sintering temperatures in FDM printed 316L SS. Fig. 10 shows that 1350°C had the least amount of porosity compared to a peak sinter temperature of 1200, 1250 or 1300°C.

Santamaria et al. [89] used the Hall-Petch parameters on the microstructure to predict the strength from the microstructure image of the FDM printed 316L SS. Samples were sintered at 1350°C for 2 h which lead to an average grain size of 40 ± 23 μm, ASTM grain size number of 7.5 and an average grain aspect ratio of 3.0 ± 2.4. The authors attributed the lower yield strength to the large grain size from the Hall-Petch relationship. It was noted that this metric can produce inconsistent results in the sample has high porosity.

Microstructure examination done by Abe et al. [75] on as-sintered and aging heat treated 17-4 PH specimens showed a little change in microstructure, deeming the aging heat treatment not effective. The bright and dark grains seen in Fig. 11 are martensite and ferrite phases respectively with the small spherical nodes noted to be SiO₂. Samples were sintered at 1280°C with a dwell time of 2 h.

Vetter et al. [83] identified the printing defects in 1.2083 tool steel samples sintered at 1250°C for 3 hours. As highlighted in Fig. 12, printing layer lines are still evident in the FDM printed tool steel after sintering which resulted in large pores.

Ortega Varela de Seijas et al. [71] sintered 316L SS samples in a vacuum furnace at 1350°C for 10 s, 30 s, 1 min, 4 min, and 6 min. Average samples density significantly increased from 66.4 to 99.9% as the sinter time increased from 10 s to 6 min. Samples sintered in the vacuum furnace had higher Austenitic and less Ferrite in the microstructure compared to samples sintered in the refractory ballast.

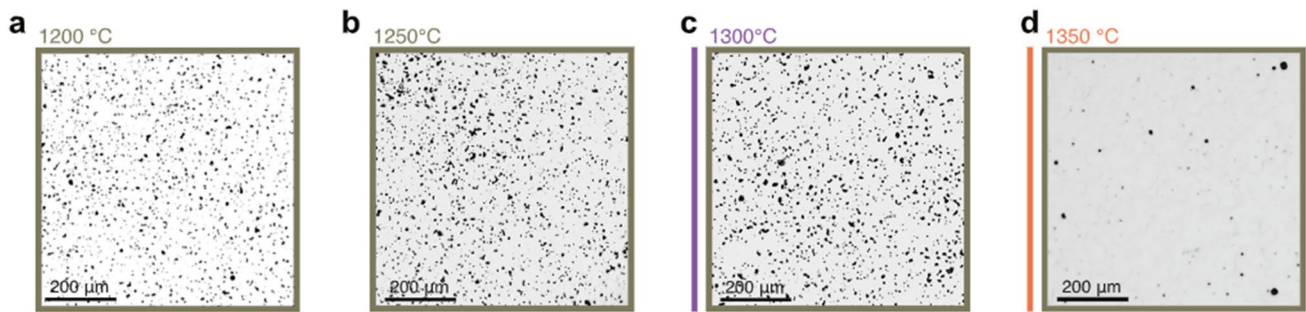


Fig. 10 Comparison of peak sintering temperatures for FDM printed 316L SS at (a) 1200°C (b) 1250°C (c) 1300°C (d) 1350°C [67]

Fig. 11 Microstructure results from 17-4PH (a) as-sintered and (b) heat treated specimens [75]

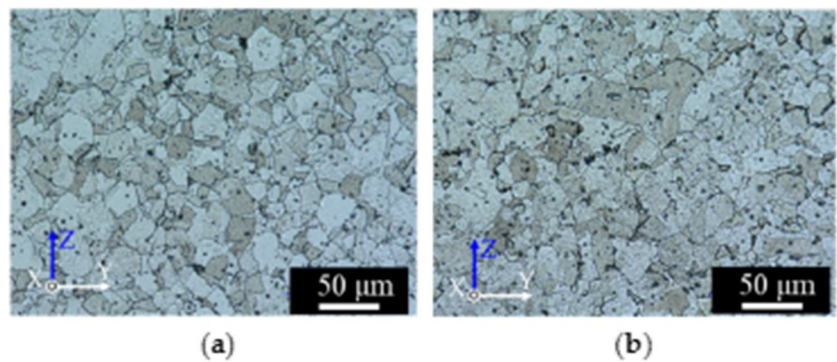


Fig. 12 Printing defects in FDMm sintered 1.2083 tool steel [83]

4.2 Post-sinter treatment

Wang et al. [42] performed hot isostatic pressing (HIPing) at 80 MPa for 1 h on sintered tensile samples. A significant porosity reduction from 7.5 to 0.3 vol% was achieved. HIPing was also found in increase in the tensile strength from 412 to 540 MPa while removing anisotropic properties. Pellegrini et al. [80] investigated the effects of H900 and H1150 aging treatment for FDMm 17-4PH SS printing by 2 different printing brands. An 18.9% and 34.4% increase in hardness was achieved after the H900 heat aging process. The authors noted that this was likely due to a Cu-precipitate enrichment

in the martensite matrix. A 17.4 and 18.0% decrease in hardness was achieved after performing the H1150. A decrease in hardness can happen when the feedstock has high levels of austenite which will decrease during heat treatment. An 18.4 and 34.3% reduction in porosity was found after the H900 heat treatment and a 21.3 and 32.2% reduction in porosity occurred after the H1150 [80]. A similar study by Bouaziz et al. [101] showed that H900 heat treatment increased the UTS by 16%.

Forcellese et al. [104] performed heat treatments of the sintered parts to increase the martensite grain structure. The authors used a solubilization heat treatment for 1 h at 1040°C followed an aging treatment at 482°C for 1 h. Condruz et al. [118] subjected FDMm printed 17-4PH SS to a quenching heat treatment. Samples were quenched at 1040°C for 40 min and air cooled to room temperature. Samples were either tempered at 550°C or 450°C for 90 min.

Table 5 SMAT parameters [102]

Post-treatment parameters	SMAT high
Ball material	100Cr6 steel
Ball diameter	3 mm
Processing time	30 min
Power and frequency of the generator	30% and 20 kHz

Outside of the common heat treatment techniques, Chemkhi et al. [102] used SMAT to increase strain hardening on the surface of the samples. The parameters seen in Table 5 allow for a 700 MPa reduction in residual stresses within the samples.

4.2.1 Sintering process and mechanical properties

In this section, Table 6 summarizes key numerical data for sintering used in the literature.

5 Research gaps and challenges

To increase the viability of AM in the industrial setting, further experimentation in process optimization is needed. Optimization of the filament making, printing, debinding and sintering is needed to create strong and repeatable parts.

Table 6 Literature studies FDMm sintering and mechanical properties information

Study	Material	Sintering temp.	Sintering hold length	UTS	Percentage of ASTM standard	Shrinkage x/y-direction	Shrinkage z-direction	Density achieved
Mousapour et al. [35]	316L SS	1310–1400°C	1 h, 6 h, 12 h	-	-	10% avg.		87–92%
Liu et al. [60]	316 SS	1360°C	2 h	441 MPa	85.1%	17% avg.		92.2%
Quarto et al. [61]	316 SS	-	-	-	-	17%	20%	95%
Sadaf et al. [62]	316L SS	1380°C	3 h	520 MPa	100.4%	11%	15%	91–93%
Kurose et al. [63]	316L SS	1280°C	2 h	453 MPa	87.5%	14–15%	15–17%	92.9%
Hassan et al. [64]	316L SS	1350°C	1 h	-	-	12.7% avg.		7.11 g/cm ³ +/- 0.13
Damon et al. [65]	316L SS	1380°C	3 h	≈500 MPa	96.5%	20% avg.		98.5%
Thompson et al. [66]	316L SS	1360°C	2 h	-	-	16.3%	17.4%	95%
Wagner et al. [67]	316L SS	1200, 1250, 1300, 1350	3 h	561 MPa	108.3%	-	-	96%
Wang et al. [42]	316L SS	1320°C	2 h	412 MPa	79.5%	-	-	92.5%
Caminero et al. [68]	316L SS	1380°C	1.5 h	495, 497 MPa	95.6–95.9%	-	-	94.01–99.49%
Obadimu et al. [87]	316L SS	-	-	-	-	16.5%	19.8%	-
Kedziora et al. [88]	316L SS	-	-	314 MPa	60.6%	21.35%***	26%***	-
Gong et al. [90]	316L SS	-	-	465 MPa	89.8%	13 - 18%	18%-23%	98.5%
Tosto et al. [112]	316L SS	-	-	443.9 MPa	85.7%	-	-	90.33%
Santamaria et al. [89]	316L SS	1350°C	2 h	524 MPa	101.2%	-	-	98.73%
Parenti et al. [69]	316L SS	1340°C	1 h	-	-	-	-	-
Ortega Varela de Seijas et al. [71]	316L SS	1350°C	10 s, 30 s, 1 min, 4 min and 6 min	-	-	-	-	64.7–99.9%
Jimbo and Tateno [92]	316L SS	1350°C	2 h	-	-	28.2% volume shrinkage		-
Abe et al. [75]	17-4PH SS	1280°C	2 h	1100 MPa, 1140MPa	79.8–82.7%	15%	16.8–17.1%	97.9%, 98.1%
Watson et al. [76]	17-4PH SS	1404–1440°C	-	1042 MPa	97.4%**	18.6%***	19.5%***	98%

Table 6 (continued)

Study	Material	Sintering temp.	Sintering hold length	UTS	Percentage of ASTM standard	Shrinkage x/y-direction	Shrinkage z-direction	Density achieved
Gonzalez-Gutierrez et al. [78]	17-4PH SS	1380°C	5 h	-	-	16%	20%	95.7%
Jiang and Ning [79]	17-4PH SS	-	-	-	-	15.2%	14.1%	-
Pellegrini et al. [80]	17-4PH SS	1100°C	1 h	-	-	-	-	97.6%
Pellegrini et al. [80]	17-4PH SS	1300°C	3 h	-	-	-	-	97.8%
Atatreh et al. [93]	17-4PH SS	1300-1380°C	-	1018 MPa	73.8%	-	-	-
Kedziora et al. [88]	17-4PH SS	-	-	496 MPa	36.0%	19.5%***	20%***	-
Tosto et al. [91]	17-4PH SS	-	-	942.6 MPa*	68.4%	19.72%	25.20%	95.7%
Lavecchia et al. [94]	17-4PH SS BASF Ultrafuse	1300°C	3 h	472-898 MPa	34.2–65.1%	-	-	88.9-95.5%
Lavecchia et al. [94]	17-4PH SS Markforged	1100°C	26–27 h Total	436-836 MPa	31.6–60.6%	-	-	97.6–98.7%
Leonard and Tammawil-liams [113]	17-4PH SS	1300°C	-	-	-	15.20%	15.66%	-
Henry et al. [97]	17-4PH SS	-	26 h Total	-	-	20%***	20%***	-
Chemkhi et al. [102]	17-4PH SS	1300°C	27 h Total	-	-	-	-	-
Galati and Minetola [103]	17-4PH SS	-	-	-	-	72.6% volume shrinkage		88.2–90.9%
Watson et al. [105]	17-4PH SS	1304–1390°C	48 h Total	1042 MPa	75.5%	-	-	98%
Fongsamootr et al. [99]	17-4PH SS	-	-	852 MPa	81.69%**	-	-	-
Suwanpreecha and Manon-ukul [100]	17-4PH SS	1200°C	3 h	-	-	-	-	-
Vetter et al. [83]	1.2083 Tool Steel	1250°C	3 h	-	-	12.7% avg.		7.4 g/cm ³
Rahimi and Zamani [82]	4605 Steel	1200°C	1.5 h	278–522 MPa	18.7–35.3% [114]	-	-	96.3%
Mousapour et al. [35]	High Carbon Iron	1310–1400°C	1 h, 6 h, 12 h	-	-	10% avg.		87–92%
Charpentier et al. [84]	High Carbon Tool Steel	1250°C	0.5 h, 2 h, 3.5 h, 5 h	-	-	-		97.22–97.36%
Giberti et al. [109]	AISI 630 Stainless Steel	1360°C	-	-	-	12.1% avg.		-

*Corrected tensile strength based on real load bearing area [91]

**Author Compared to Wrought 17-4PH Stainless Steel sample

***Software shrinkage compensation values [76, 88]

Listed below are challenges and gaps in the research that need further investigation:

1. Investigation into different binder packing capacities and processes to create an optimally dense and printable filament.
2. Investigation into different filament manufacturing techniques to create the metallurgically dense and most chemically consistent filament
3. Further optimization of printing parameters to maximize the strength, density and tolerances of a print
4. Experimentation into debinding techniques such as temperature, temperature acceleration rate, environment and time to see the effects on porosity and other defects during debinding.
5. Experimentation into effects of sintering parameters such as peak sinter temperature, peak sinter hold length, sub-sinter temperature, temperature acceleration rate, sintering atmosphere and cooldown rate.
6. Optimization of the heat treatment process from an optimized sintering process. Testing different heat treatment cycles on sintered parts can improve mechanical properties of FDM sintered parts.

Funding This work was supported by the National Science and Engineering Research Council (NSERC).

Declarations

Competing interests The authors declare no competing interests.

References

1. Kumar S (2022) Additive manufacturing classification
2. Markforged Metal 3D Printer: the metal X 3D printing system. <https://markforged.com/3d-printers/metal-x>. Accessed 29 Sep 2022
3. Gu W, Styger E, Warner DH (2020) Assessment of additive manufacturing for increasing sustainability and productivity of smallholder agriculture. *3D Print Addit Manuf* 7:300–310. <https://doi.org/10.1089/3dp.2020.0022>
4. Mardis NJ (2018) Emerging technology and applications of 3D printing in the medical field. *Mo Med* 115(4):368–373
5. Chohan JS, Singh R, Boparai KS (2019) Fused deposition modelling - applications and advancements. In: *Additive Manufacturing Applications and Innovations*, pp 131–136 LCCN 2018027130
6. Additive Manufacturing for spare parts. <https://www2.deloitte.com/nl/nl/pages/energy-resources-industrials/articles/industry40-additive-manufacturing-for-spare-parts.html>. Accessed 29 Sep 2022
7. Foshammer J, Sjøberg PV, Helo P, Ituarte IF (2022) Identification of aftermarket and legacy parts suitable for additive manufacturing: a knowledge management-based approach. *Int J Prod Econ*:253. <https://doi.org/10.1016/j.ijpe.2022.108573>
8. The Virtual Foundry Inc (2020) About us. <https://thevirtualfoundry.com/about-us/>. Accessed 14 Oct 2021
9. Agarwal R, Sharma S, Gupta V et al (2023) Additive manufacturing: Materials, technologies, and applications. In: *Additive Manufacturing; Advanced Materials and Design Techniques*, pp 77–99. <https://doi.org/10.1201/9781003258391>
10. Godec D, Portolés L, Blasco JR et al (2022) Introduction to additive manufacturing. In: *A Guide to Additive Manufacturing*, pp 1–15. <https://doi.org/10.1007/978-3-031-05863-9>
11. Lalegani Dezaki M, Mohd Ariffin MKA, Hatami S (2021) An overview of fused deposition modelling (FDM): research, development and process optimisation. *Rapid Prototyp J* 27:562–582
12. Types of 3D Printing in Metal. <https://markforged.com/resources/learn/design-for-additive-manufacturing-metals/metal-additive-manufacturing-introduction/types-of-3d-printing-metal>. Accessed 30 Sep 2022
13. Toyserkani E, Sarker D, Ibhado OO et al (2021) Additive manufacturing process classification, applications, trends, opportunities, and challenges. In: *Metal Additive Manufacturing*. Wiley, pp 4–5. <https://doi.org/10.1002/9781119210801>
14. Greguric L (2023) How much does a metal 3D printer cost? | All3DP Pro. In: All3DP's Content Academy. <https://all3dp.com/2/how-much-does-a-metal-3d-printer-cost/>. Accessed 22 Apr 2023
15. Suwanpreecha C, Manonukul A (2022) A review on material extrusion additive manufacturing of metal and how it compares with metal injection moulding. *Metals (Basel)* 12. <https://doi.org/10.3390/met12030429>
16. Savini A, Savini GG (2015) A short history of 3D printing, a technological revolution just started. In: *Proceedings of the 2015 ICOHTEC/IEEE international history of high-technologies and their socio-cultural contexts conference, HISTELCON 2015. The 4th IEEE Region 8 Conference on the History of Electrotechnologies*. Institute of Electrical and Electronics Engineers Inc, pp 1–4. <https://doi.org/10.1109/HISTELCON.2015.7307314>
17. Fused filament fabrication – simply explained | All3DP. <https://all3dp.com/2/fused-filament-fabrication-fff-3d-printing-simply-explained/>. Accessed 6 May 2023
18. What is atomic diffusion additive manufacturing (ADAM)? <https://markforged.com/resources/learn/3d-printing-basics/3d-printing-processes/what-is-atomic-diffusion-additive-manufacturing-adam>. Accessed 6 May 2023
19. Atomic diffusion additive manufacturing (ADAM) - simply explained - Pick 3D Printer. <https://pick3dprinter.com/atomic-diffusion-additive-manufacturing/#>. Accessed 6 May 2023
20. Gong C, Djouda JM, Hmima A et al (2021) 2D characterization at submicron scale of crack propagation of 17-4PH parts produced by Atomic diffusion additive manufacturing (ADAM) process. In: *Procedia Structural Integrity*. Elsevier B.V., pp 13–19
21. Ramazani H, Kami A (2022) Metal FDM, a new extrusion-based additive manufacturing technology for manufacturing of metallic parts: a review. *Prog Additive Manuf* 7:609–626
22. Chakravorty D (2020) Cura tutorial: master Cura Slicer Software settings. In: ALL3DP. <https://all3dp.com/1/cura-tutorial-software-slicer-cura-3d/>. Accessed 12 Oct 2021
23. New filament means you can print metal on any 3D printer - 3D printing industry. <https://3dprintingindustry.com/news/new-can-print-metal-3d-printer-85255/>. Accessed 28 Sep 2022
24. Rapidia - Fast & Simple Metal 3D Printing. <https://www.rapidia.com/>. Accessed 29 Sep 2022
25. Desktop Metal Studio 3D Printer | Affordable Metal 3D Printing. <https://proto3000.com/product/desktop-metal-studio-3d-printer-2-2/>. Accessed 29 Sep 2022

26. The best metal 3D printers of 2022 | All3DP Pro. <https://all3dp.com/1/3d-metal-3d-printer-metal-3d-printing/>. Accessed 28 Sep 2022
27. Markforged Inc. Markforged Metal 3D Printer: the Metal X 3D printing system. <https://markforged.com/3d-printers/metal-x>. Accessed 29 Sep 2022
28. Siemiński P (2021) Introduction to fused deposition modeling. In: Additive Manufacturing. Elsevier, pp 217–265
29. Original Prusa 3D printers directly from Josef Prusa. <https://www.prusa3d.com/>. Accessed 29 Sep 2022
30. Anycubic Kobra Series – ANYCUBIC 3D Printing. <https://www.anycubic.com/collections/kobra-series>. Accessed 29 Sep 2022
31. CREALITY - Official Website, Leading 3D Printer Supplier & Manufacturer. <https://www.creality.com/>. Accessed 29 Sep 2022
32. The Virtual Foundry Metal 3D Printer, Print Pure Metal Parts | The Virtual Foundry. <https://shop.thevirtualfoundry.com/en-ca/collections/metal-3d-printers-and-printing-accessories/products/metal-3d-printer-print-pure-metal-parts?variant=40627055296684>. Accessed 28 Sep 2022
33. Kristiawan RB, Imaduddin F, Ariawan D et al (2021) A review on the fused deposition modeling (FDM) 3D printing: filament processing, materials, and printing parameters. *Open Eng* 11:639–649
34. Nabipour M, Akhoundi B, Bagheri Saed A (2020) Manufacturing of polymer/metal composites by fused deposition modeling process with polyethylene. *J Appl Polym Sci* 137:48717. <https://doi.org/10.1002/app.48717>
35. Mousapour M, Salmi M, Klemettinen L, Partanen J (2021) Feasibility study of producing multi-metal parts by Fused Filament Fabrication (FFF) technique. *J Manuf Process* 67:438–446. <https://doi.org/10.1016/j.jmapro.2021.05.021>
36. GIONDA A (2020) How to debind parts produced by additive manufacturing. <https://www.tav-vacuumfurnaces.com/blog/57/en/debinding-additive-manufacturing>. Accessed 12 Oct 2021
37. Lu H (2014) Preliminary mechanical characterization of the low-cost metal 3D printing
38. Spiller S, Kolstad SO, Razavi SMJ (2022) Fabrication and characterization of 316L stainless steel components printed with material extrusion additive manufacturing. *Proc Struct Integr* 42:1239–1248. <https://doi.org/10.1016/j.prostr.2022.12.158>
39. Terry S, Fidan I, Tantawi K (2019) Dimensional analysis of metal powder infused filament - low cost metal 3D printing. In: 30th Annual international solid freeform fabrication symposium, pp 535–537
40. The Virtual Foundry Inc (2020) Webinar: all about Sintering Filamet™. In: Webinar Series https://www.youtube.com/watch?v=CAv6SrjXibQ&t=2480s&ab_channel=TheVirtualFoundry%2CInc. Accessed 14 Oct 2021
41. Zhou C, Wu F, Tang D et al (2023) Effect of subcritical-temperature heat treatment on corrosion of SLM SS316L with different process parameters. *Corros Sci* 218. <https://doi.org/10.1016/j.corsci.2023.111214>
42. Wang Y, Zhang L, Li X, Yan Z (2021) On hot isostatic pressing sintering of fused filament fabricated 316L stainless steel – evaluation of microstructure, porosity, and tensile properties. *Mater Lett* 296. <https://doi.org/10.1016/j.matlet.2021.129854>
43. Varmaziar S, Atapour M, Hedberg YS (2022) Corrosion and metal release characterization of stainless steel 316L weld zones in whey protein solution. *Npj Mater Degrad* 6. <https://doi.org/10.1038/s41529-022-00231-7>
44. Type 316/316L stainless steels explained. <https://www.thoughtco.com/type-316-and-316l-stainless-steel-2340262>. Accessed 30 Sep 2022
45. 17-4 PH stainless steel in AMS 5604, UNS S17400 - sheet, plate, and round bar. <https://www.upmet.com/products/stainless-steel/17-4-ph>. Accessed 30 Sep 2022
46. Berns H, Theisen W (2008) Ferrous materials: Steel and cast iron. Springer, Berlin Heidelberg. <https://doi.org/10.1007/978-3-540-71848-2>
47. Tractus3D FDM 3D printing - fused deposition modeling also known as FFF. <https://tractus3d.com/knowledge/learn-3d-printing/fdm-3d-printing/>. Accessed 12 Oct 2021
48. Kishore V, Hassen AA (2021) Polymer and composites additive manufacturing: material extrusion processes. In: Additive Manufacturing. Elsevier, pp 183–199
49. Sola A, Trinchi A (2023) Basic principles of fused deposition modeling. In: Fused Deposition Modeling of Composite Materials. Elsevier, pp 7–39
50. Mishra A, Srivastava V, Gupta NK (2021) Additive manufacturing for fused deposition modeling of carbon fiber–polylactic acid composites: the effects of process parameters on tensile and flexural properties. *Funct Compos Struct* 3:7–8. <https://doi.org/10.1088/2631-6331/ac3732>
51. Çevik Ü, Kam M (2020) A review study on mechanical properties of obtained products by FDM method and metal/polymer composite filament production. *J Nanomater*:3–4. <https://doi.org/10.1155/2020/6187149>
52. The Virtual Foundry filament for 3D printing metal on an FDM system - 3D Printing Industry. <https://3dprintingindustry.com/news/the-virtual-foundry-filament-for-3d-printing-metal-on-an-fdm-system-140705/>. Accessed 30 Sep 2022
53. Rane K, Strano M (2019) A comprehensive review of extrusion-based additive manufacturing processes for rapid production of metallic and ceramic parts. *Adv Manuf* 7:155–173. <https://doi.org/10.1007/s40436-019-00253-6>
54. Strano M, Rane K, Briatico Vangosa F, Di Landro L (2019) Extrusion of metal powder-polymer mixtures: melt rheology and process stability. *J Mater Process Technol* 273. <https://doi.org/10.1016/j.jmatprotec.2019.116250>
55. Kan X, Yang D, Zhao Z, Sun J (2021) 316L FFF binder development and debinding optimization. *Mater Res Express* 8. <https://doi.org/10.1088/2053-1591/ac3b15>
56. Roshchupkin S, Kolesov A, Tarakhovskiy A, Tishchenko I (2021) A brief review of main ideas of metal fused filament fabrication. In: *Materials Today: Proceedings*. Elsevier Ltd, pp 2063–2067
57. Metal Powders: Particle Characterization. [Microtrac.com. https://www.microtrac.com/applications/particle-characterization-of-metal-powders/](https://www.microtrac.com/applications/particle-characterization-of-metal-powders/). Accessed 7 Mar 2023
58. Nurhuda AI, Supriadi S, Whulanza Y, Saragih AS (2021) Additive manufacturing of metallic based on extrusion process: a review. *J Manuf Process* 66:231–232
59. Mashekov S, Bazarbay B, Zhankeldi A, Mashekova A (2021) Development of technological basis of 3d printing with highly filled metal-poly-dimensional compositions for manufacture of metal products of complex shape. *Metalurgija* 60:355–358
60. Liu B, Wang Y, Lin Z, Zhang T (2020) Creating metal parts by fused deposition modeling and sintering. *Mater Lett* 263. <https://doi.org/10.1016/j.matlet.2019.127252>
61. Quarto M, Carminati M, D’Urso G (2021) Density and shrinkage evaluation of AISI 316L parts printed via FDM process. *Mater Manuf Process* 36:1535–1543. <https://doi.org/10.1080/10426914.2021.1905830>
62. Sadaf M, Bragaglia M, Nanni F (2021) A simple route for additive manufacturing of 316L stainless steel via fused filament fabrication. *J Manuf Process* 67:141–150. <https://doi.org/10.1016/j.jmapro.2021.04.055>

63. Kurose T, Abe Y, Santos MVA et al (2020) Influence of the layer directions on the properties of 316L stainless steel parts fabricated through fused deposition of metals. *Materials* 13. <https://doi.org/10.3390/ma13112493>
64. Hassan W, Farid MA, Tosi A et al The effect of printing parameters on sintered properties of extrusion-based additively manufactured stainless steel 316L parts. <https://doi.org/10.1007/s00170-021-07047-w/Published>
65. Damon J, Dietrich S, Gorantla S et al (2019) Process porosity and mechanical performance of fused filament fabricated 316L stainless steel. *Rapid Prototyp J* 25:1319–1327. <https://doi.org/10.1108/RPJ-01-2019-0002>
66. Thompson Y, Gonzalez-Gutierrez J, Kukla C, Felfer P (2019) Fused filament fabrication, debinding and sintering as a low cost additive manufacturing method of 316L stainless steel. *Addit Manuf* 30:3–7. <https://doi.org/10.1016/j.addma.2019.100861>
67. Wagner MA, Engel J, Hadian A et al (2022) Filament extrusion-based additive manufacturing of 316L stainless steel: effects of sintering conditions on the microstructure and mechanical properties. *Addit Manuf* 59. <https://doi.org/10.1016/j.addma.2022.103147>
68. Caminero MÁ, Romero Gutiérrez A, Chacón JM et al (2022) Effects of fused filament fabrication parameters on the manufacturing of 316L stainless-steel components: geometric and mechanical properties. *Rapid Prototyp J* 28:2004–2026. <https://doi.org/10.1108/RPJ-01-2022-0023>
69. Parenti P, Cataldo S, Annoni M (2018) Shape deposition manufacturing of 316L parts via feedstock extrusion and green-state milling. *Manuf Lett* 18:6–11. <https://doi.org/10.1016/j.mfglet.2018.09.003>
70. Lotfizarei Z, Mostafapour A, Barari A et al (2023) Overview of debinding methods for parts manufactured using powder material extrusion. *Addit Manuf* 61. <https://doi.org/10.1016/j.addma.2022.103335>
71. Ortega Varela de Seijas M, Bardenhagen A, Rohr T, Stoll E (2023) Indirect induction sintering of metal parts produced through material extrusion additive manufacturing. *Materials* 16. <https://doi.org/10.3390/ma16020885>
72. Moritzer E, Elsner CL, Schumacher C (2021) Investigation of metal-polymer composites manufactured by fused deposition modeling with regard to process parameters. *Polym Compos* 42:6065–6079. <https://doi.org/10.1002/pc.26285>
73. Gonzalez-Gutierrez J, Godec D, Kukla C et al (2017) Shaping, debinding and sintering of steel components via fused filament fabrication. In: 16 th International Scientific Conference on Production Engineering-CIM2017 Croatian Association of Production Engineering, pp 2–7
74. Burkhardt C, Hampel S, Sondermaschinenbau H (2021) Fused Filament Fabrication (FFF) of 316L green parts for the MIM process. In: *World PM2016 – AM - Deposition Technologies*
75. Abe Y, Kurose T, Santos MVA et al (2021) Effect of layer directions on internal structures and tensile properties of 17-4ph stainless steel parts fabricated by fused deposition of metals. *Materials* 14:1–12. <https://doi.org/10.3390/ma14020243>
76. Watson A, Belding J, Ellis BD (2020) Characterization of 17-4 PH processed via bound metal deposition (BMD). In: *Minerals, metals and materials series*. Springer, pp 205–216
77. Godec D, Cano S, Holzer C, Gonzalez-Gutierrez J (2020) Optimization of the 3D printing parameters for tensile properties of specimens produced by fused filament fabrication of 17-4PH stainless steel. *Materials* 13. <https://doi.org/10.3390/ma13030774>
78. Gonzalez-Gutierrez J, Arbeiter F, Schlauf T et al (2019) Tensile properties of sintered 17-4PH stainless steel fabricated by material extrusion additive manufacturing. *Mater Lett* 248:165–168. <https://doi.org/10.1016/j.matlet.2019.04.024>
79. Jiang D, Ning F (2022) Material extrusion of stainless-steel plate-lattice structure: Part shrinkage, microstructure, and mechanical performance. *Manuf Lett* 33:712–718
80. Pellegrini A, Lavecchia F, Guerra MG, Galantucci LM (2023) Influence of aging treatments on 17–4 PH stainless steel parts realized using material extrusion additive manufacturing technologies. *Int J Adv Manuf Technol*. <https://doi.org/10.1007/s00170-023-11136-3>
81. Wu G, Langrana NA, Sadanji R, Danforth S (2001) Solid free-form fabrication of metal components using fused deposition of metals. *Mater Des* 23:98–105
82. Rahimi AH, Zamani J (2022) Development of a feedstock for additive manufacturing of 4605 steel compact by FDMS process. *Trans Ind Inst Metals* 75:3087–3093. <https://doi.org/10.1007/s12666-022-02678-3>
83. Vetter J, Huber F, Wachter S et al (2022) Development of a material extrusion additive manufacturing process of 1.2083 steel comprising FFF printing, solvent and thermal debinding and sintering. In: *Procedia CIRP*. Elsevier B.V., pp 341–346
84. Charpentier N, Barrière T, Bernard F et al (2022) PIM-like EAM of steel-tool alloy via bio-based polymer. In: *Procedia CIRP*. Elsevier B.V., pp 477–482
85. Ait-Mansour I, Kretzschmar N, Chekurov S et al (2020) Design-dependent shrinkage compensation modeling and mechanical property targeting of metal FFF. *Prog Additive Manuf* 5:51–57. <https://doi.org/10.1007/s40964-020-00124-8>
86. Schumacher C, Moritzer E (2021) Stainless steel parts produced by fused deposition modeling and a sintering process compared to components manufactured in selective laser melting. *Macromol Symp* 395. <https://doi.org/10.1002/masy.202000275>
87. Obadimu SO, Kasha A, Kourousis KI (2022) Tensile performance and plastic anisotropy of material extrusion steel 316L: influence of primary manufacturing parameters. *Addit Manuf* 60. <https://doi.org/10.1016/j.addma.2022.103297>
88. Kedziora S, Decker T, Museyibov E et al (2022) Strength properties of 316L and 17-4 PH stainless steel produced with additive manufacturing. *Materials* 15. <https://doi.org/10.3390/ma15186278>
89. Santamaria R, Salasi M, Bakhtiari S et al (2022) Microstructure and mechanical behaviour of 316L stainless steel produced using sinter-based extrusion additive manufacturing. *J Mater Sci* 57:9646–9662. <https://doi.org/10.1007/s10853-021-06828-8>
90. Gong H, Snelling D, Kardel K, Carrano A (2019) Comparison of stainless steel 316L parts made by FDM- and SLM-based additive manufacturing processes. *Jom* 71:880–885. <https://doi.org/10.1007/s11837-018-3207-3>
91. Tosto C, Tirillò J, Sarasini F et al (2022) Fused deposition modeling parameter optimization for cost-effective metal part printing. *Polymers (Basel)* 14:3264. <https://doi.org/10.3390/polym14163264>
92. Jimbo K, Tateno T (2019) Shape contraction in sintering of 3d objects fabricated via metal material extrusion in additive manufacturing. *Int J Autom Technol* 13:354–360. <https://doi.org/10.20965/ijat.2019.p0354>
93. Atatreh S, Alyammahi MS, Vasilyan H et al (2023) Evaluation of the infill design on the tensile properties of metal parts produced by fused filament fabrication. *Results Eng* 17. <https://doi.org/10.1016/j.rineng.2023.100954>
94. Lavecchia F, Pellegrini A, Galantucci LM (2023) Comparative study on the properties of 17-4 PH stainless steel parts made by metal fused filament fabrication process and atomic diffusion

- additive manufacturing. *Rapid Prototyp J* 29:393–407. <https://doi.org/10.1108/RPJ-12-2021-0350>
95. Alkindi T, Alyammahi M, Susantyoko RA, Atatreh S (2021) The effect of varying specimens' printing angles to the bed surface on the tensile strength of 3D-printed 17-4PH stainless-steels via metal FFF additive manufacturing. *MRS Commun* 11:310–316. <https://doi.org/10.1557/s43579-021-00040-0>
 96. Lawrence BD, Henry TC, Phillips F et al (2023) High-cycle tension-tension fatigue performance of additively manufactured 17–4 PH stainless steel. *Int J Adv Manuf Technol*. <https://doi.org/10.1007/s00170-023-11146-1>
 97. Henry TC, Morales MA, Cole DP et al (2021) Mechanical behavior of 17-4 PH stainless steel processed by atomic diffusion additive manufacturing. <https://doi.org/10.1007/s00170-021-06785-1/Published>
 98. Bjørheim F, La Torraca Lopez IM (2021) Tension testing of additively manufactured specimens of 17-4 PH processed by bound metal deposition. *IOP Conf Ser Mater Sci Eng* 1201:012037. <https://doi.org/10.1088/1757-899x/1201/1/012037>
 99. Fongsamootr T, Thawon I, Tippayawong N et al (2022) Effect of print parameters on additive manufacturing of metallic parts: performance and sustainability aspects. *Sci Rep* 12. <https://doi.org/10.1038/s41598-022-22613-2>
 100. Suwanpreecha C, Manonukul A (2022) On the build orientation effect in as-printed and as-sintered bending properties of 17-4PH alloy fabricated by metal fused filament fabrication. *Rapid Prototyp J* 28:1076–1085. <https://doi.org/10.1108/RPJ-07-2021-0174>
 101. Bouaziz MA, Djouda JM, Chemkhi M et al (2021) Heat treatment effect on 17-4PH stainless steel manufactured by atomic diffusion additive manufacturing (ADAM). In: *Procedia CIRP*. Elsevier B.V., pp 935–938
 102. Chemkhi M, Djouda JM, Bouaziz MA et al (2021) Effects of mechanical post-treatments on additive manufactured 17-4PH stainless steel produced by bound powder extrusion. In: *Procedia CIRP*. Elsevier B.V., pp 957–961
 103. Galati M, Minetola P (2019) Analysis of density, roughness, and accuracy of the atomic diffusion additive manufacturing (ADAM) process for metal parts. *Materials* 12:4122. <https://doi.org/10.3390/ma12244122>
 104. Forcellese P, Mancina T, Simoncini M, Bellezze T (2022) Investigation on corrosion resistance properties of 17-4 PH bound metal deposition as-sintered specimens with different build-up orientations. *Metals (Basel)* 12. <https://doi.org/10.3390/met12040588>
 105. Watson A, Belding J, Ellis BD (2020) Characterization of 17-4 PH processed via bound metal deposition (BMD). In: *TMS 2020 149th Annual meeting & exhibition supplemental proceedings*. Springer International Publishing, Cham, pp 205–216
 106. Banerjee S, Joens CJ (2019) Debinding and sintering of metal injection molding (MIM) components. In: *Handbook of Metal Injection Molding*. Elsevier, In, pp 129–171
 107. Hamidi MFFA, Harun WSW, Khalil NZ, et al (2017) Study of solvent debinding parameters for metal injection moulded 316L stainless steel. In: *IOP Conference Series: Materials Science and Engineering*. Institute of Physics Publishing, pp 2–10. doi:10.1088/1757-899X/257/1/012035
 108. Ghadimi H, Jirandehi AP, Nemati S et al (2023) Effects of printing layer orientation on the high-frequency bending-fatigue life and tensile strength of additively manufactured 17-4 PH stainless steel. *Materials* 16. <https://doi.org/10.3390/ma16020469>
 109. Giberti H, Strano M, Annoni M (2016) An innovative machine for Fused Deposition Modeling of metals and advanced ceramics. In: *MATEC Web of Conferences*. pp 1–5. <https://doi.org/10.1051/mateconf/20160003>
 110. Stainless Steel Melting Point Revealed - thyssenkrupp Materials (UK). <https://www.thyssenkrupp-materials.co.uk/stainless-steel-melting-points.html>. Accessed 29 Sep 2022
 111. 17-4 Stainless steel properties | KVA Stainless. <http://www.kvastainless.com/17-4.html>. Accessed 29 Sep 2022
 112. Tosto C, Tirillò J, Sarasini F, Cicala G (2021) Hybrid metal/polymer filaments for fused filament fabrication (FFF) to print metal parts. *Appl Sci (Switzerland)* 11:1. <https://doi.org/10.3390/app11041444>
 113. Léonard F, Tammas-Williams S (2022) Metal FFF sintering shrinkage rate measurements by X-ray computed tomography. *Nondestruct Test Evaluation* 37:631–644. <https://doi.org/10.1080/10589759.2022.2085702>
 114. Kinetics MIM 4605 Low Alloy Steel (Quenched + Tempered) datasheet. http://www.lookpolymers.com/polymer_Kinetics-MIM-4605-Low-Alloy-Steel-Quenched-Tempered.php. Accessed 2 May 2023
 115. AK Steel 17-4 PH® Precipitation hardening stainless steel. Condition H 925 https://www.matweb.com/search/datasheet_print.aspx?matguid=f653f7356a524e69916049d0a64a11fc. Accessed 22 Apr 2023
 116. Angelo B Ravisankar PC (2019) Introduction to steels - processing, properties, and applications. *LCC TN730 .A58 2019 | DDC 669/.142-dc23*
 117. ASM Material Data Sheet. <https://asm.matweb.com/search/SpecificMaterial.asp?bassnum=mq316q>. Accessed 21 Feb 2023
 118. Condruz MR, Paraschiv A, Puscasu C (2018) Heat treatment influence on hardness and microstructure of ADAM manufactured 17-4 PH AM
 119. Ding S, Zou B, Wang P, Ding H (2019) Effects of nozzle temperature and building orientation on mechanical properties and microstructure of PEEK and PEI printed by 3D-FDM. *Polym Test* 78:1–2. <https://doi.org/10.1016/j.polymertesting.2019.105948>
 120. Cura Extrusion Multiplier: 5 ways to improve your prints | All3DP. <https://all3dp.com/2/extrusion-multiplier-cura-ways-to-improve-your-prints/>. Accessed 29 Sep 2022
 121. Biroş MT, Ledenyák D, Andó M (2022) Effect of FDM infill patterns on mechanical properties. *Polym Test* 113:1–3. <https://doi.org/10.1016/j.polymertesting.2022.107654>
 122. Sri Ardion F, Sukanto H, Triyono J (2019) Analisis pengaruh infill overlap terhadap karakteristik produk hasil 3D printing dengan menggunakan material Poly Lactic Acid (PLA). *Mekanika: Jurnal Ilmiah Mekanika* 18:56
 123. Rankouhi B, Javadpour S, Delfanian F, Letcher T (2016) Failure analysis and mechanical characterization of 3D printed ABS with respect to layer thickness and orientation. *J Fail Anal Prevent* 16:467–481. <https://doi.org/10.1007/s11668-016-0113-2>
 124. Ding S, Zou B, Wang P, Ding H (2019) Effects of nozzle temperature and building orientation on mechanical properties and microstructure of PEEK and PEI printed by 3D-FDM. *Polym Test* 78. <https://doi.org/10.1016/j.polymertesting.2019.105948>
 125. Yaman U (2018) Shrinkage compensation of holes via shrinkage of interior structure in FDM process. *Int J Adv Manuf Technol* 94:2187–2197. <https://doi.org/10.1007/s00170-017-1018-2>
 126. Nizam MAN, Bin MK, Bin IK, Yap TC (2022) The effect of printing orientation on the mechanical properties of FDM 3D printed parts. In: Abdul Sani AS, Osman Zahid MN, Mohamad Yasin MR et al (eds) *Enabling Industry 4.0 through Advances in Manufacturing and Materials*. Springer Nature Singapore, Singapore, pp 75–77
 127. Ansari AA, Kamil M (2021) Effect of print speed and extrusion temperature on properties of 3D printed PLA using fused deposition modeling process. In: *Materials Today: Proceedings*. Elsevier Ltd, pp 5462–5466

128. Masood SH (2014) Advances in fused deposition modeling. *Comp Mater Process* 10:71–75. <https://doi.org/10.1016/B978-0-08-096532-1.01002-5>
129. Korkut V, Yavuz H (2020) Enhancing the tensile properties with minimal mass variation by revealing the effects of parameters in fused filament fabrication process. *J Brazil Soc Mech Sci Eng* 42. <https://doi.org/10.1007/s40430-020-02610-0>

Publisher's Note Springer Nature remains neutral with regard to jurisdictional claims in published maps and institutional affiliations.

Springer Nature or its licensor (e.g. a society or other partner) holds exclusive rights to this article under a publishing agreement with the author(s) or other rightsholder(s); author self-archiving of the accepted manuscript version of this article is solely governed by the terms of such publishing agreement and applicable law.